Skoltech

Skolkovo Institute of Science and Technology

A NOVEL STRAIGHTFORWARD WET PULLING TECHNIQUE TO FABRICATE CARBON NANOTUBE FIBERS

Doctoral Thesis

by

MARIIA ZHILIAEVA

DOCTORAL PROGRAM IN MATERIALS SCIENCE AND ENGINEERING

Supervisor

Professor Albert G. Nasibulin

Moscow - 2021

I hereby declare that the work presented in this thesis was carried out by myself at Skolkovo Institute of Science and Technology, Moscow, except where due acknowledgement is made, and has not been submitted for any other degree.

Candidate Mariia Zhiliaeva

Supervisor Prof. Albert Nasibulin

Abstract

The growing demand for wearable electronics requires flexible and stretchable conductive materials. Among them, carbon nanotubes are recognized for their outstanding mechanical, electrical, optical properties and chemical stability. This work introduces a novel technique of carbon nanotube fiber fabrication, which was named Wet Pulling. The method allows straightforward fiber production out of carbon nanotube thin films, collected on a filter after the synthesis or deposited onto any substrate. It relies on a combination of film and solvent properties.

We examined a wet-pulled fiber formation from pristine and modified carbon nanotube films. It is shown that the electrical characteristics of the as-produced fibers are determined by the type of liquid employed in their formation, which defines the carbon nanotubes packing degree. The obtained specific strength (0.6–0.8 N/tex), toughness (up to 127 J/g) and specific conductivity (0.5–1.2 kS·m^2/kg) are in many cases comparable with published data for fibers produced by more resource-consuming methods. These, in combination with the simplicity of our method and high piezoresistive gauge factor of 14 (for untwisted fibers at a 1% elongation), make the carbon nanotubes fibers promising components in future applications of stretchable electronics and robotics.

The wet pulling technique has prominent advantages that make it a promising candidate for both small and large-scale production of carbon nanotube fibers with desired properties. The method is also easily adaptive to different kinds of carbon nanotubes and allows rapid fabrication of both active and passive flexible electronic components. As one of the illustrative examples of the active ones, the piezoresistive wet-pulled carbon nanotubes sensor was designed and extensively studied. It is characterized by an adjustable force range coupled with high sensitivity to enable the detection of a wide range of forces and displacements limited by the experimental setup only. We have demonstrated the applicability of the developed unit in tactile

sensing, displacement sensing, and nanophone vibration monitoring system and evaluated its force sensing characteristics, *i.e.* displacement/force input and resistance/mechanical response. In the experiments it measures 0-115 N force range within 2.5 mm displacement. Moreover, the sensor demonstrates good linearity, low hysteresis, and stability when tested over 10 000 cycles. The developed sensor suits multiple applications in the field of soft and transparent sensors, nanophones, actuators, and other robotics devices for both regular and extreme environments, *e.g.* deep underwater and radioactive environment.

Acknowledgments

This thesis would not have been possible without the support and guidance of my teachers, colleagues, family, and friends.

First and foremost, I would like to express my gratitude and appreciation to my thesis advisor, professor Albert Nasibulin, for helping me to find my research focus, for his supervision, guidance, support, and patience. It has been an honor and inspiration to work with him over the past years.

I have been lucky to participate in and learn from a wonderful community of scientists. A special thank to the colleagues from the Laboratory of Nanomaterials (LNM) of the Center for Photonics and Quantum Materials of the Skolkovo Institute of Science and Technology (Skoltech). In particular, I wish to acknowledge the close collaboration with Eugene Shulga, Oyedamola Asiyanbola, Dima Mironov, Fedor Fedorov, Stepan Romanov, and Andrey Starkov.

Additional support has come from my friends Aysylu Askarova, Dina Bek, Natalia Glazkova, Alena Alexeeva, Anastasia Fursova, Anna Fefilova, Adeniy Adebayo, for heart-to-heart tea talks and making my studies at Skoltech a memorable one.

I would like to thank Clement Fortin, for the insights into my thesis, and inspirational conversations over all my study at Skoltech.

Thanks, Mom and Dad, Natalia and Alexey, for teaching me as a child and passing your love of numbers and engineering thinking on to me. A special big thank to my Mom who spreads her love and cares about my daughter, Toma, while I was working on my thesis. To my sister, Dasha, who I just love so much.

My final, and biggest, thank you is to my husband, Peter, for his unwavering, support and encouragement, as well as his belief in me.

Mariia Zhiliaeva,

December, Moscow 2021

List of Publications

I.   **Zhilyaeva MA**, Shulga E V., Shandakov SD, Sergeichev I V., Gilshteyn EP, Anisimov AS, Nasibulin AG. A Novel Straightforward Wet Pulling Technique to Fabricate Carbon Nanotube Fibers. Carbon 2019;15069–75.

II. Shandakov SD, Kosobutsky A V., Vershinina AI, Sevostyanov OG, Chirkova IM, Russakov DM, Lomakin M V., Rybakov MS, Glushkova T V., Ovcharenko EA, **Zhilyaeva MA**, Nasibulin AG. Electromechanical Properties of Fibers Produced from Randomly Oriented SWCNT Films by Wet Pulling Technique. Mater. Sci. Eng. B Solid-State Mater. Adv. Technol. 2021;269115178.

III. **Zhilyaeva MA**, Asiyanbola AA, Lomakin MV, Mironov DM, Voloskov BS, Mikladal B, Tsetsereukou DO, Fedorov FS, Shandakov SD, Nasibulin AG. Tunable Force Sensor Based on Single-walled Carbon Nanotube Fiber for Fine Mechanical and Acoustic Technologies. Submitted to Soft Robotics journal.

Author's contribution

I. The author is mainly responsible for the work. The author was responsible for the method investigation, fiber characterization, design applications, and writing the manuscript.

II. The author was responsible for fiber manufacturing methods and sample preparation techniques, as well as tutoring the electromechanical experiments.

III. The author is mainly responsible for the work. The author created the sensors' designs and manufacturing techniques, tutored and designed all experiments. The author was responsible for writing the manuscript.

Table of contents

List of symbols and abbreviations

3D – three dimensional

CNF – carbon nanofibers

CNT – carbon nanotube

CVD – chemical vapor deposition

DMSO - dimethyl sulfoxide

FEM - finite element method

FT-IR - Fourier-transform infrared spectroscopy

GF – gauge factor

IR - infrared

MWCNT – multiwalled carbon nanotube

PDMS – polydimethylsiloxane

PLA – polylactide

PU - polyurethane

SEM – scanning electron microscopy

SWCNT – single-walled carbon nanotube

TEM - transmission electron microscopy

THF – tetrahydrofuran

TPU - thermoplastic polyurethane

WP – wet pulling

1. Introduction

1.1. Carbon nanotubes fibers

CNTs are good candidates to be used in wearable electronics because of their outstanding strength and good electrical conductivity, combined with their chemical stability [1]. Although CNTs possess remarkable properties, the devices made of individual CNTs are quite challenging in fabrication. CNTs are usually used in the form of fibers [2], arrays [3], or films [4]. Electrically and thermally conductive enduring CNT fibers can be utilized in many applications: flak jacket [5], lightweight composite [6], additive manufacturing [7], space elevator [8], smart textile and wearable electronics [9,10], solar panels [11,12], sensors [13], actuators [14], flexible electronic components like electrodes [15], transmissions lines [16], capacitors [17], and passive components [18–20]. In general, a CNT integrity in fibers is determined by van der Waals forces, an innate strength, and surface tension [21].

Di et al. [22] classify fiber fabrication approaches into four groups: (i) Surfactant-based coagulation spinning [23], which introduces a polymeric binder between CNTs to form fibers and requires a rotating stage and injection mechanism with a controlled velocity. (ii) Direct spinning [24,25], where fiber is formed during a CNT synthesis in the reactor [26]. It requires a carefully designed CVD reactor with many optimized parameters such as a reaction temperature, gas flow rates, identity of a carbon source, a catalyst precursor, a promoter and a carrier gas [24]. (iii) Forest spinning [2,27], which pulls and rearranges vertically grown CNTs into the horizontally aligned fiber. This process requires a spinnable CNT array (CNT forests with a certain structure and geometry) and a variable-speed motor. (iv) Liquid-crystalline spinning, which uses the nature of CNTs to form liquid crystals under certain conditions. Besides special equipment (mixing machine, stainless steel syringes, capillary tubes, rotating shear cells, pneumatic pistons, coagulation baths, and vacuum ovens) it is time-consuming and requires meeting a long list of parameters (pressure, temperature, viscosity, etc.) [28].
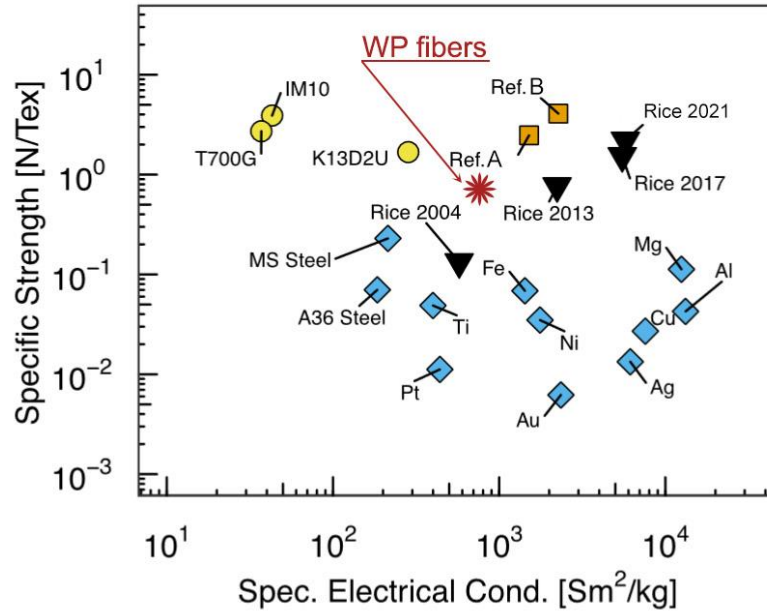
Figure 1. The best current materials performance. Based on *Taylor et.al.* [29] analysis.

Figure 1 is based on *Taylor et.al.* [29] analysis. Ref. A[26] and Ref. B[30] – are the best nowadays CNT fibers results. Rice 2004, 2013, 2017, 2021 – results obtained at Rice University over the years. Yellow rounds are carbon fibers, blue rhombs – metals. Figure 1 shows that the WP fibers possessed compatible properties. Since it is the very first presentation of the WP fibers, there is a great potential to enhance their properties by the WP process optimization and different treatments/doping/twisting (see how Rice's fiber's properties have been improved over time).

All methods require time-consuming and complex procedures, while there is a need for a straightforward way for rapid prototyping and fabrication, which has the potential to be scaled up. Therefore, the fabrication of CNT fibers is a complex process with many requirements and limitations, which need to be simplified to open daily applications.

Herein, we propose a novel technique for the CNT fiber production, which was named Wet Pulling (WP). Its implementation provides scientists and engineers with a simple and undemanding CNT fiber fabrication method. The general procedure claims to soak a CNT film with a liquid/solvent (e.g., ethanol), then pull a film from the edge. The

use of solvent is a common approach for fiber densification.[31,32] Crucial phenomena in the WP process are film folding by surface tension and densification during solvent evaporation. With a given liquid, the diameters of the fibers can be controlled by changing geometrical parameters of the film such as width and thickness. The film with larger width or thickness folds into the fiber with a larger diameter.[33] The method is universal for different types of CNT films and can be easily implemented in any laboratory practically without special equipment. The WP method requires tweezers, ethanol (or another solvent[27]), and CNT film with a suitable thickness. The WP method opens up broad opportunities for manufacturing and rapid prototyping tactile, bend, vibration and force sensors. They can be utilized for robotic grippers, earth tremors recording, building shrinkage analysis, hydrophone devices, medical surgery, artificial skin and many more.

1.2. Force sensing devices

The design of new force-sensing devices serves as one of the core drivers for technologies and application areas related to smart prosthetics, remote control, and robot grippers.[34–37] In particular, force sensors with adjustable and wide sensing ranges are important for applications in lifting variable loads, the rehabilitation of patients, vital signs monitoring, body movements monitoring, and many others.[34,38–40] Recent studies in this field are aimed at miniaturization of the sensing devices and utilization of stretchable substrates.[34] Still, the fabrication process is fraught with onerous material processing requirements that demands rather costly equipment.[35] Conventional manufacturing methods yield brittle units which can typically accommodate a strain of less than 5% for optimum performance.[40,41] To mitigate problems pertaining to the strain limits of available sensing technologies, future generations of co-robot platforms are expected to include sensors with architectures that are elastically soft and would even ensure compliance matching to human tissue.[42,43]

Conventional force sensors, like strain gauges, employ piezoresistive materials and often contain composites or dual physically cross-linked hydrogels,or capacitors.[40,44–48]

Also, piezoresistive force sensors based on carbon nanomaterials have attracted huge attention because they enable the achievement of a wide force operation range while offering stability and uniformity of sensor response, higher reliability, and sustainability. However, while the bearing capacity of a force sensor depends primarily on the force sensor's modulus[40,47,48] such new or existing materials do not allow to achieve significant changes in sensor performance.[40,49,50]

Alternatively, the force-sensing devices with high modulus can be made from mechanical architectures, like diaphragms, springs, or cantilevers. Still, such devices do not meet the flexibility criteria needed for delicate applications in bio-robotics for tissue identification.[45,51,52] New approaches to force sensing for soft robotics systems also include wavy circuits and soft microfluidics with conductive liquids.[40,43,53,54] Unlike the wavy electronics circuitry, microfluidics systems are limited to conductive liquids such as electrolytic solutions or liquid-phase metal alloys, e.g. a gallium-indium liquid-phase alloy.[43] Fabrication of either wavy circuitry or microfluidic channels still requires lithography or other delicate fabrication technologies.

One of the most promising materials, SWCNT fibers, possesses all necessary properties to create superb sensors: good electrical conductivity, high mechanical strength and flexibility, supreme chemical stability, tiny dimensions, and facile fabrication pathway. CNT fibers have a wide range of electrical responsivity for strain and force-sensitive devices.[55,56] Moreover, a recently developed novel CNT fiber manufacturing technique, called WP [33], enables the simplified production of a tactile sensor with an adjustable force range. Still, the sensor architecture requires components of particular flexural rigidity to adjust its modulus.[34] Usually force adjustment is achieved by changing springs or plates of different stiffness, layer jamming, or even fluids dome.[40,57,58]

In this work, we propose an adjustable piezoresistive force sensor based on a WP single-walled carbon nanotube (SWCNT) fibers with flexural rigidity attained by mounting the sensor with stiffener plates of different thickness. Thus, one may vary the

elastic properties of the sensor assembly and therefore provide an adjustable force-sensing range up to 104 N with high cyclic stability (>10000 cycles) during dynamic loading conditions, good linearity, low hysteresis characteristics. Finally, the sensors have been applied for vibration monitoring system or as a sensitive part of special sound recording system, which we denote further as a nanophone.

2. Experimental

2.1. CNT synthesis

For the demonstration of the method, we utilized SWCNT films produced by the floating catalyst (aerosol) CVD method, collected on a nitrocellulose filter.[59-61] The key element is a quartz tubular reactor heated to 880 °C. SWCNTs were synthesized on the surface of iron catalyst particles floating in a gas flow (**Figure 2a**). Carbon monoxide (800 ccm/min) was a carbon source, ferrocene vapor (with a partial pressure of around 0.7 Pa) was a catalyst precursor. The SWCNTs were collected downstream of the reactor on a nitrocellulose filter.[59] The deposited films consisted of as-grown randomly oriented SWCNTs with a typical length of 20–40 µm, which are free from surfactants and possess good conductivity.[62] The surface density was determined based on a thermogravimetric analysis[63], and the content of catalytic iron particles among the synthesis products was measured to be around 17 wt%. The SWCNTs in the deposited films were highly entangled and formed a two-dimensional network with cell sizes of the order of 10–100 nm (**Figure 2b**).
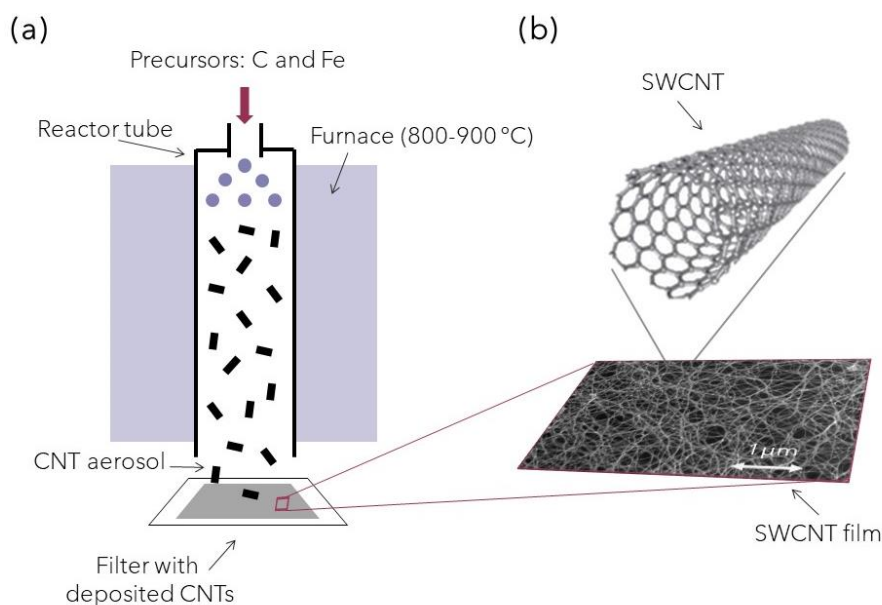
Figure 2. (a) Scheme of the aerosol CVD synthesis of SWCNT films. (b) SEM image of a deposited SWCNT film.

2.2. WP technique, solvents, treatments, and twisting

For the WP method demonstration and experiments we utilized SWCNT films produced directly by floating catalyst CVD synthesis, and by filtering the CNT dispersion. Filter with deposited CNTs were cut to the of 0.5 × 1.5 cm^2 stripes. Then, the film was soaked with solvent for a few seconds. For the major experiments (not for solvent and doping tests) the films were impregnated with ethanol (Ethanol 95%, Bryntsalov-A Company). We choose ethanol because it was very good at separating SWCNTs film from both glass surface and filter. At the same time, it is a widely available solvent with low toxicity.

In addition, the results of the experiments with different solvents and as well as treatment and doping are also demonstrated in the "Results and discussion" chapter. Each point of the presented data was obtained by averaging results from 4 to 7 samples. Ethanol (95.6%), acetone (99%), DMSO (99.9%) and THF (97%) were used to test different solvents. Fibers with twist angles of about 30° were prepared by using stepper motor at a speed of 10 rpm for comparative analysis. Part of the fibers was treated for one minute with a 0.1 M aqueous solution of $HAuCl_4$ diluted with ethanol or acetone to form a 10 mM solution. All experiments were conducted at the room temperature.

2.3. Structural and optical properties

The structural and optical properties of the films were examined using TEM with JEOL JEM-2100 instrument, SEM S-3400N, Hitachi, FTIR spectrometer Brucker Vertex 80v, and Raman spectroscopy (Horiba LabRam HR 800). For optical measurements, we used optical microscope (Leica DM4500). For morphology investigations of CNT fibers, FEI Versa DualBeam scanning electron microscope was used.

2.4. Electromechanical tests and fiber characterization

Electromechanical test performance requires a SWCNT fiber setup into the testing machine. To avoid fiber damage and to achieve solid contacts, the holder was designed and 3D printed with side connections (columns) between upper and lower parts. The fiber ends were glued with thin copper wires on the surface of the holders (**Figure 3**) using electrically conductive adhesive Mechanic MCN-DJ002. After the installation of a holder with a fiber to the testing machine, these connections were cut with nippers.

(a)   (b)   (c)
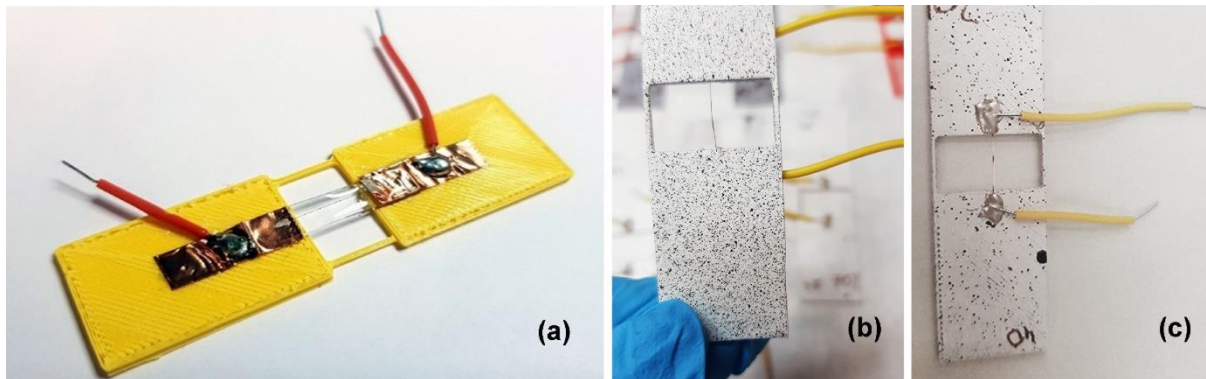
Figure 3. Photographs of the fibers on holders. (a) The encapsulated fiber on a holder with attached wires. (b) The back side of the holder is painted white with black dots for Digital Image Correlation. (c) The front side of the holder with fiber (not encapsulated) glued together with wires.

In order to investigate the influence of the SWCNT film dimensions on the resulted fiber properties, the following experimental approach was performed. We prepared the first sample set of the filters with the different thicknesses of SWCNT films: 23 nm (80% transmittance at 550 nm), 37 nm (70% transmittance), 53 nm (60% transmittance), 72 nm (50% transmittance), 95 nm (40% transmittance) with the fixed width of 5 mm; the second set of samples with different widths: 2, 4, 5, 6, 8, and 10 mm with the fixed thickness of 53 nm (60% transmittance). The film thickness error is 0,2-0,5%, width error 0,1 mm. Both of them are less than the size of the experimental point. Therefore, they are not presented on plots. Assuming the fiber has an elliptical cross-section, the

effective diameter is defined as $d=(d_{min}d_{max})1/2$, where d_{min} and d_{max} are minimum and maximum diameters, observed in an optical microscope. During the experiments, 110 CNT fibers were prepared and investigated in total. Minimum five replicates with the same width and thickness were prepared for each statistical test. For morphology investigations of CNT fibers, FEI Versa DualBeam scanning electron microscope was used.

The SWCNT fibers were simultaneously tested (Electromechanical testing system INSTRON 5969) with two-wires resistance measurements (Digital Multimeter Keysight 34410A) using the special 3D printed holders (**Figure 3**). Fibers were firmly glued with thin copper wires onto the holder using CircuitWorks® Conductive Epoxy, Product #CW2400, which has the volume resistivity <0.00001 ohm-m. Then the holders were installed in the electromechanical testing system. The tensile test was performed with the load cell of 10 N, the cross-head speed of 5 mm/min, and the gauge length of 10 mm. The pictures of the encapsulated and not encapsulated fiber with the holder are shown in **Figure 3a** and **Figure 3b,c,** correspondingly.

Due to the small dimensions of fibers, we could not use an extensometer available in our laboratory. To ensure the accuracy of the strain measurement, the holders were painted white with small black dots (**Figure 3b**) for using Digital Image Correlation (DIC) system VIC-3DTM. The results were corrected according to the DIC tests, which demonstrated only 2% discrepancy with the tensile machine data.

The specific strength is determined as a strength (force per unit area at failure), obtained during the tensile tests, normalized by a fiber density. It requires the knowledge of the fiber masses, which were calculated by an empirical equation given in [64]. Specific conductance was calculated with four-wire resistance measurements (Digital Multimeter Keysight 34410A) for a cross-sectional area unit of the fiber. The latter was determined both by the thickness of the film and by its packing density in the fiber. The dependence of the packing density was defined as the ratio of the cross-sectional areas of the film and fiber, on the thickness of the film. The thicknesses of the

SWCNT films were calculated from the film transmittance at 550 nm using the equation of $h = -239 \cdot \lg(T)$, [65] where h is the thickness of the SWCNT film (nm). It is worth noting that Zhilyaeva et al. [66] (published in 2019) estimated the film thickness using equation $h = -417 \cdot \lg(T)$ [67]. But in 2020 Ermolaev et al. [65] updated the coefficient in the equation. In this dissertation all values are recalculated according to the most recent study.

The fatigue test was done on a fatigue testing system Instron 8801. Encapsulated (see chapter 3.3.1) in PDMS (SYLGARD®, silicone elastomer base 184 and curing agent 184) fiber experienced 10 000 load cycles with 8% strain, 10 N load cell, 30 mm/min crosshead speed, 10 mm gauge length. In order to increase an elastic range, the fiber was pre-strained at 10%.

Sensing opportunities of the SWCNT fibers were obtained by pulse measuring. Encapsulated in PDMS (SYLGARD®, silicone elastomer base 184 and curing agent 184) SWCNT fiber was glued with CircuitWorks® Conductive Epoxy (Product #CW2400) to the wires and attached to the human wrist and neck zones. Digital Multimeter Keysight 34410A measured the resistance changing of the fiber. For pulse measurements, fatigue tests and three-point bending tests we use fibers, made from 2 mm wide strip with a 53 nm thickness. For all sensor experiments we used fibers made from a 5 mm wide strip with a 93 nm thickness SWCNTs film. The relative changes of the resistance calculated as $\Delta R/R_0 = (R_s - R_0)/R_0$, where R_0 and R_s are resistances without and with applied strain, respectively.

An impinger, 1 cm in diameter, was used to simulate a finger tap in all mechanical experiments: the three-point bending, fatigue, and step load tests. An electromechanical testing system Instron® ElectroPlus E3000 was used for displacement-controlled experiments. During all tests, there was a maximum deflection of 2.5 mm, applied loads with the 50 kN load cell and 3 mm/min crosshead speed.

We measured the resistance and corresponding resistance changes of the fiber in a two-electrode configuration, using Digital Multimeter Keithley 2000 (Tektronix company©). The relative changes of the resistance of fiber sensing element (sensitivity) were calculated as $\frac{\Delta R}{R_0} = \frac{R_s - R_0}{R_0}$, where R_0 and R_s are resistances without and under applied load conditions, respectively.

2.5. Acoustic test

Sound sensing capabilities of the SWCNT fibers were demonstrated by recording a fragment of the Georges Bizet - "Les Toreadors" from Carmen Suite No. 1 (more details in chapter 3.4.4). All recordings are monophonic. From the obtained data, spectrograms were generated using a windowed Fourier transform. To construct spectrograms and waveforms, a Python™ script (Librosa and Matplotlib libraries) was used.

Nanophone electrical circuit. To test the nanophone, the circuit in **Figure 4** was assembled. It amplifies the nanophone voltage signal variations.
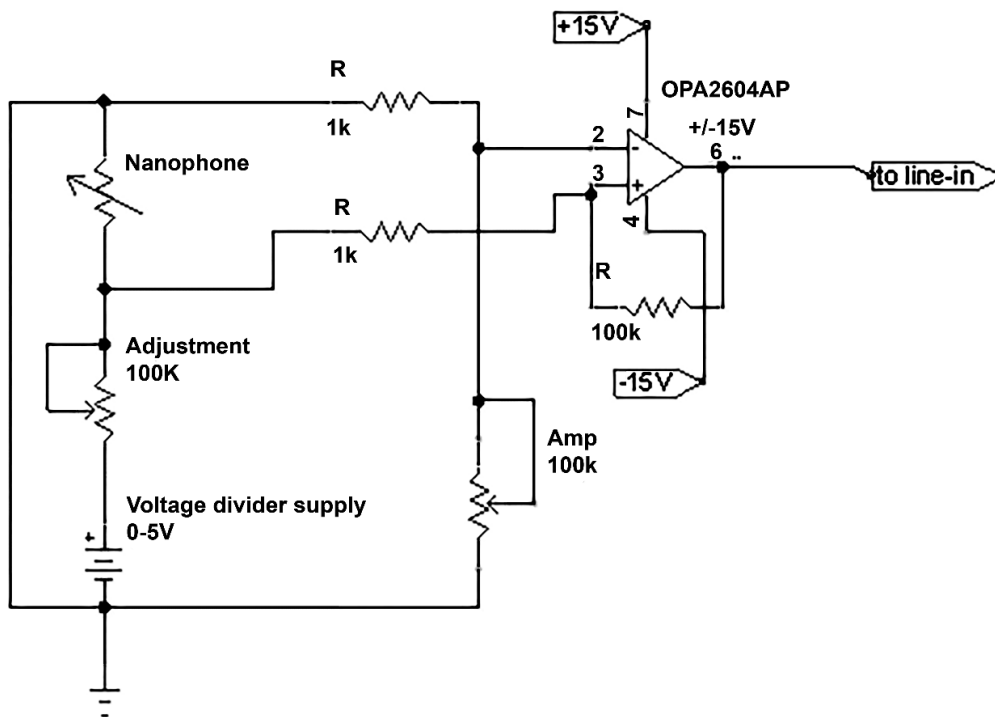
Figure 4. Nanophone electrical circuit.

The circuit used a low-noise OPA2604AP operational amplifier, powered by a +/- 15V bipolar power supply. The operational amplifier was connected according to a differential circuit, to which a signal was supplied from a voltage divider, a nanophone

was positioned in one of the arms. Due to the change in the electrical resistance in the nanophone under the action of acoustic vibrations, an electrical signal was formed at the output of the divider, which was then amplified by an operational amplifier. A 100 kΩ resistor was used to trim the divider. The divider was powered by a 0-5 V constant voltage source. The amplified signal was fed to the input of the computer sound card. The signal was recorded using the Audacity® application.

Signal recording technique. To test the nanophone, we selected well-known audio fragments of classical compositions with a duration of 1 minute. The fragments were chosen in such a way that significant differences in the amplitudes of the sound signal were present, which would make it possible to assess the sensitivity of the nanophone. The sound source was a smartphone speaker, to which a nanophone was applied in an arrangement when the fiber was opposite to the speaker. At 100 gain of the operational amplifier, pickups began to be recorded through the wires connecting the circuit to the nanophone. Due to interference, the sound could be transmitted not by propagation in the air, but by means of an electromagnetic field induced in the wires. This effect was eliminated by lowering the gain and was controlled during recording by periodically turning the power on and off at the divider.

When the power of the divider is turned off, the sound disappears, which indicates its occurrence precisely due to a change in the electrical resistance of the nanophone fiber, and not to an inductive coupling of the circuit with the electric circuits of the smartphone. An insignificant sound with the divider turned off can be heard on the test recording, however, its contribution compared to the useful signal is negligible.
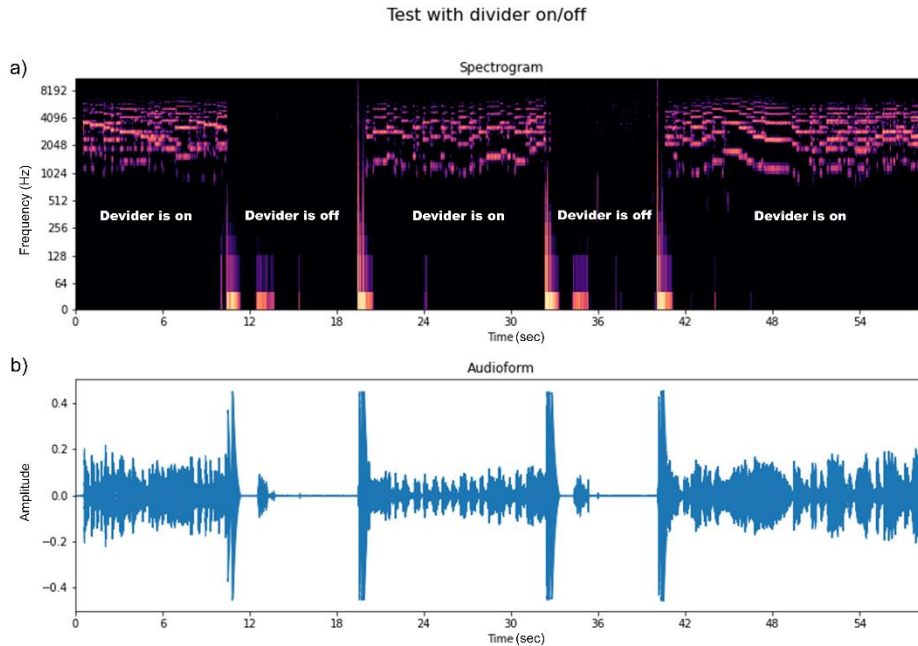
Figure 5. Acoustic test with divider turned on/off: (a) spectrogram; (b) audioform.

All fragments and the test with a divider were recorded using the same parameters. During the recording process, in addition to the useful signal, there was background noise, which was subtracted from the recording. By its nature, the noise is stationary and is presumably caused by noise from both the circuit itself and the external background electromagnetic field. A fragment of the background noise was recorded before the sound signal was sent to the nanophone, and then it was subtracted in the Audacity® program. For comparison, similar audio fragments were recorded using a conventional microphone.

3. Results and discussion

3.1. WP fiber manufacturing technique

3.1.1. Method description

The WP process is a straightforward technique. **Figure 6** illustrates the general steps. First, we carefully cut the strip out of the filter with nanotubes by a razor blade (Step 1). Next, a strip with a CNT film is covered with a solvent (Step 2). Then by using tweezers, the CNT film is pulled out of the liquid (Step 3). During pulling, the CNT film is folded by surface tension forces and forms a fiber. Right after the wet fiber leaves the solvent, (Step 4) it is placed on a dryer, where the fiber shrinks to its final dimensions, as the solvent evaporates. Crucial phenomena in the WP process are film folding and densification due to surface tension, which leads to the increase of the fiber Young's modulus and the decrease of the resistance [68]. In the advanced techniques, it can also be combined with stretching and twisting processes [69]. See the video of the WP process from the filter, https://youtu.be/B7puxNi_Djo, and after dry transfer[70], https://youtu.be/5A3FTdkBUD8.
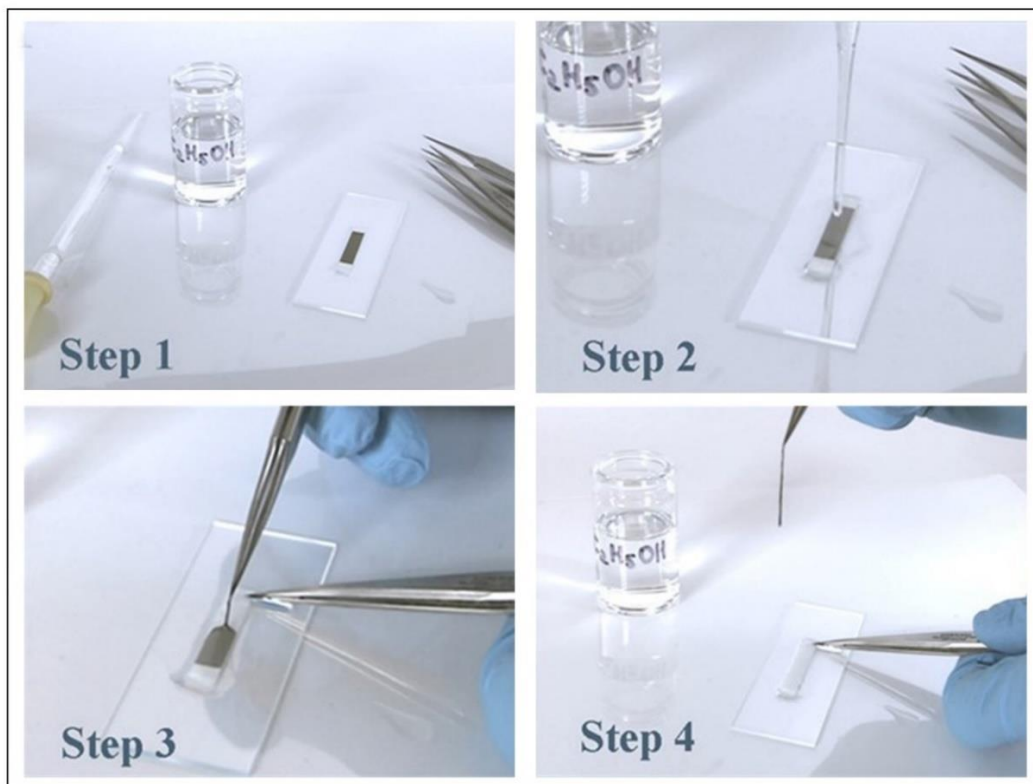
Figure 6. The procedure of SWCNT fiber production. Step 1: a SWCNT film strip of proper dimensions is prepared for the fiber formation; Step 2: impregnating the SWCNT film with ethanol; Step 3: pulling the SWCNT strip with tweezers; Step 4: Drying it up.

3.1.2. *WP production of the fibers from SWCNT film, obtained by filtering SWCNT dispersion*

Although in the previous chapter we consider only fibers fabricated from the aerosol synthesized SWCNTs, our technique was also applied to produce fibers from CNT films fabricated by other methods. The WP fibers prepared from an aqueous dispersion of commercially available SWCNTs are presented. It can be applied for multiwalled and aligned CNTs as well.

The WP method can be applied to SWCNT films, obtained by filtering CNT water dispersion. For the demonstration, we used commercial SWCNTs (TUBALL, with a

mean diameter of 1.8 nm, kindly provided by OCSiAl, Russia), dispersed in a concentration of 0.01 wt% in water with 1% wt% sodium deoxycholate (Sigma-Aldrich) and then treated for 1 hour in 10% intensity ultrasonic horn sonifier (Branson, 600w). During the sonication, a glass vial with the dispersion was immersed in an ice bath. The freshly prepared dispersion was vacuum filtered with subsequent pure water washing to minimize the amount of the surfactant (**Figure 7a**).

In comparison to the aerosol CVD synthesized SWCNTs, dispersed and filtered SWCNTs adhere to the filter stronger. We used two types of filters - HAWP04700 MF-Millipore Membrane Filter and HVLP04700 Durapore Membrane Filter PVDF membrane. Separation of the CNT film from the filter requires cutting the desired strip out of the filter, drop it into acetone filled vial (**Figure 7b**). Then mixed cellulose esters filter dissolves and PVDF filter sinks with rapid separation of the nanotube film (**Figure 7**)). Next, the CNT film should be picked by the tweezers and pulled from the solvent (**Figure 7d**). Finally, the WP fiber was placed to the holder, where it dried and shrunk to its final dimension.
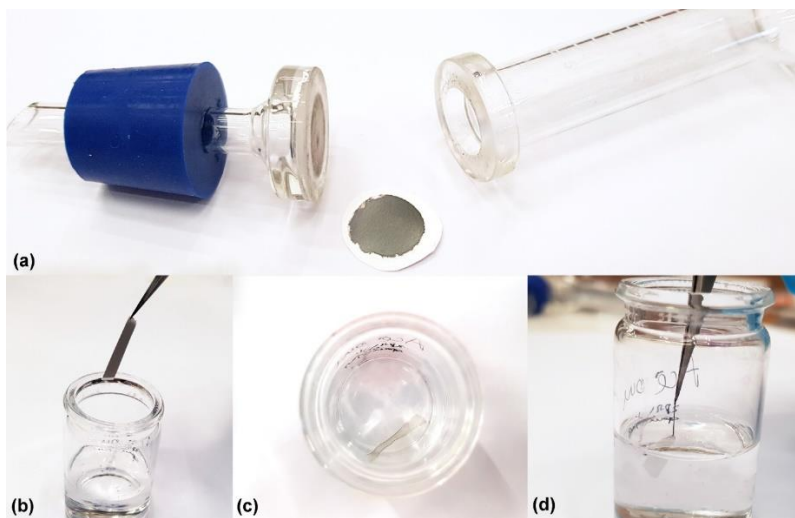
Figure 7. WP production of the fibers from SWCNT film, obtained by filtering SWCNT dispersion. (a) Vacuum filtration system after filtering the SWCNT dispersion. (b) Immerse the SWCNT strip with the filter to acetone. (c) SWCNT film in the acetone after the filter dissolved. (d) SWCNT film is pulled by the tweezers in the form of fiber.

3.1.3. Large-scale production

Figure 8 illustrates the general scheme of the scale-up production of WP CNT fibers. Firstly, the filter is entering a roll-to-roll production line (**Figure 8** Step I). Secondly, CNTs are deposited on a filter (**Figure 8** Step II). Then, the solvent impregnates the CNT film (**Figure 8** Step III). At this stage the various solvents and dopants may be applied to enhance resulted fibers' properties. The liquid flows from above, or the line passes through the solvent bath during this stage. Right after the CNT film is fully impregnated with the solvent, the film is separated from the filter (**Figure 8** Step IV). The CNT film is pulled further and folds because of liquid surface tension or twisting process. The line goes forward until the solvent evaporates completely (**Figure 8** Step V). Finally, the end-product, CNT fiber, is coiled the bobbin and ready to use for diverse applications (**Figure 8** Step VI).
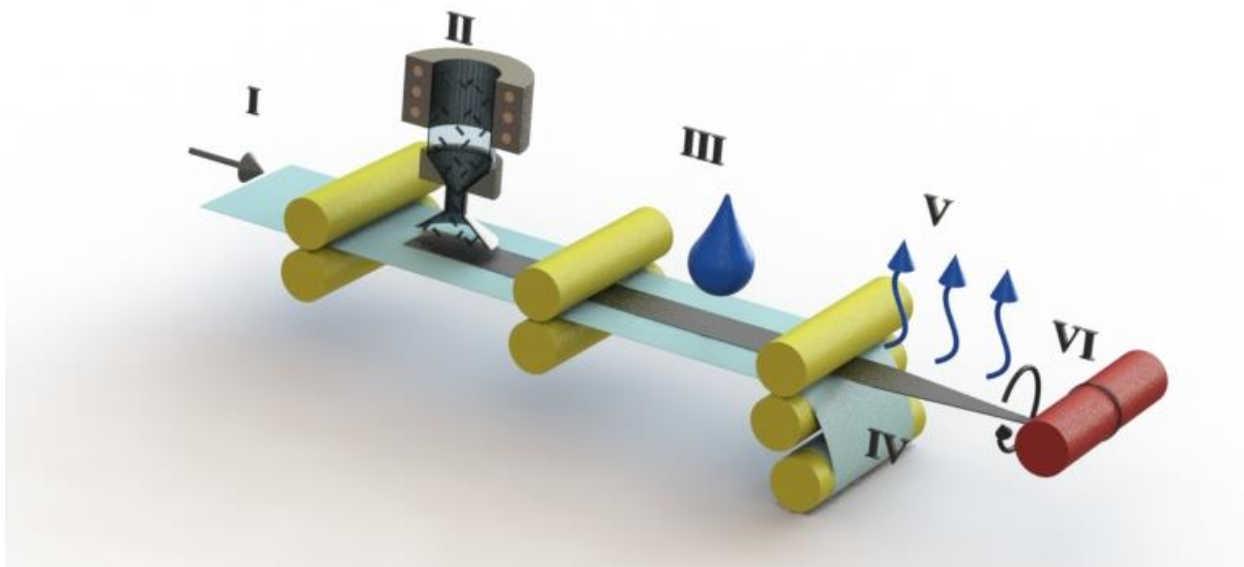
Figure 8. General scheme for the WP CNT fiber production. I) Filter supply; II) CNTs deposition on a filter; III) Solvent impregnation; IV) Filter separation; V) CNT film folding and solvent evaporation; VI) Coil the CNT fiber on the bobbin.

3.1.4. Film folding model

Here, the film folding formation model is proposed. The condition for the film folding is determined by the equilibrium of the ethanol surface tension and the film elastic forces. The fold shape is represented in **Figure 9** in the form of a thin cylindrical surface, with the thickness of a, which is small compared to the curvature radius, R.
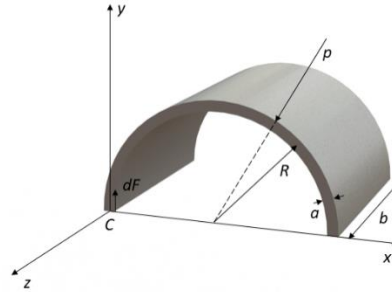
Figure 9. The representation of the CNT film fold.

The torque module with respect to the axis perpendicular to the plane of **Figure 9** and passing through point C is equal to

$$M = \int x dF = \frac{E}{R} I . \tag{1}$$

Here, E is Young's modulus of the CNT film (impregnated in ethanol), I is the second moment of area of the cross-section with width b and thickness a. Then,

$$I = \iint_{-\frac{a}{2}\ -\frac{b}{2}}^{\frac{a}{2}\ \frac{b}{2}} x^2 dx dz = \frac{a^3 b}{12}. \tag{2}$$

Taking this into account Equation 1 can be rewritten as

$$M = \frac{E a^3 b}{12R} . \tag{3}$$

The moment of external forces (surface tension of ethanol) on a thin cylindrical film relative to axis z is

$$M = \int x\, p\, \sin\varphi\, dS = \int R\, (1 - \cos\varphi)\, p\, \sin\varphi\, R\, b\, d\varphi , \tag{4}$$

where p is the pressure under the curved surface. For a thin cylindrical film (with two surfaces), the pressure is determined as

$$p = 2\sigma/R. \tag{5}$$

Here σ is the surface tension coefficient of ethanol wetting the surface of the CNT film. Combining Equation 4 and Equation 5 we get

$$M = 2\sigma R b \int_0^\pi (1 - cos\varphi) sin\varphi \, d\varphi = 4\sigma R b. \tag{6}$$

Then Equation 3 can be rewritten as

$$R^2 = \frac{Ea^3}{48\sigma}, \tag{7}$$

and the fold diameter (the characteristic fold size, l = 2R) is related to Young's modulus, CNT film thickness, and solvent surface tension coefficient as follows

$$l = \sqrt{\frac{Ea^3}{12\sigma}}. \tag{8}$$

It should be noted, that Equation 8 was obtained for a thin film of a rectangular cross-section. The restriction of a small film thickness relative to the bending radius assumes a small deformation along the surface of the film and, therefore, an elastic deformation. To be sure, the same dependence was used in estimating the minimum height of the vertical CNT forest strip on the substrate, at which the capillary forces lead to its folding onto the substrate in a work of Tawfick et al.[71]

Figure 10 demonstrates two possible shapes of the film folds. In the first case when film segments do not touch each other after folding, the distance between the folds is equal to the bending diameter (Figure 10a), l. According to Equation 8, the maximum packing density value for this case is determined by the ratio: $a/l = (12\sigma/aE)^{1/2}$. Quantitative evaluation assumes the film thickness to be of a = 37, 72, 95 nm and Young's modulus E = 6, 15, 21 GPa, respectively. The Young's modulus of the film was evaluated from Young's modulus of the fiber. The latter was calculated from the initial elastic segment of the stress curve (Figure 10b). For film thicknesses of 37, 72, and 95

nm, the fibers have an average value of Young's modulus 6, 15, 21 GPa, correspondingly. Taking into account the experimental values of the packing density of an order of 0.1, the difference between Young's moduli of the fiber and film should be within the same order of magnitude. Thus, Young's moduli of the CNT films are considered the same as for CNT fibers. Then, the diameter and the maximum packing density are obtained as l = 1.4, 6.2, 11.0 µm and a/l=0.026, 0.012, 0.040, respectively. On the other hand, the experimental values, a/l = 0.13, 0.10, 0.07 respectively, are several times higher than the values obtained from the folding model. This suggests a closer distance between film layers illustrated in **Figure 10b**. The layers are stacked together due to van der Waals's interaction. van der Waals force counteracts the elastic force of the film after drying. Therefore, it remains curved film parts to be in the form of a loop (**Figure 10b**).
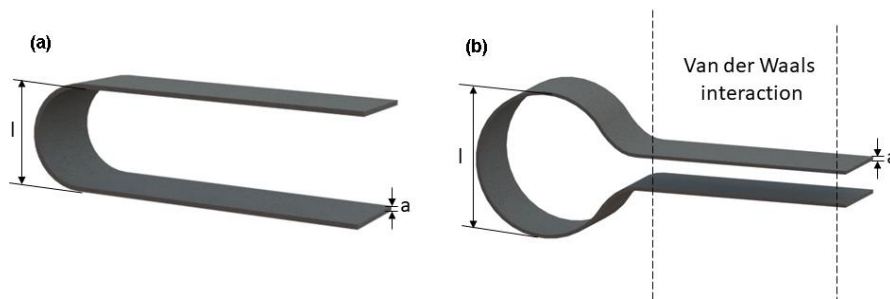
Figure 10. Possible fold shapes: (a) – the fold with alternating curved and straight segments; (b) – the fold with stacked together film layers due to van der Waals interaction.

As a result, we obtained the minimum CNT film curvature diameter and the structure of the film folding in a fiber. Within the framework of this model, the packing density is greater with a smaller radius of the loops, i.e., at a smaller film thickness, which corresponds to the experiment (see chapter 3.2.2). A part of CNT film layers is stacked together due to van der Waals forces. Those fold parts form a shape of a loop illustrated in **Figure 10b**.

3.2. WP fiber characterization

3.2.1. *Structure and dimensions*

The SWCNT film consists of free-standing randomly oriented SWCNTs. **Figure 11a** shows a scanning electron microscope (SEM) image of the pristine film, produced by the aerosol CVD method.[59] As expected, the SWCNTs quality change after the fiber fabrication was not observed (see Raman analysis in **Figure 12**).

A SWCNT fiber has a homogenous structure along the length and may be tied in 3D microstructures. **Figure 11b** shows a SEM image of fiber in the form of a knot, as an illustration of its high torsion resistance. Fabricated SWCNT fibers have a dense morphology, which is a result of effective film folding and compression during the fiber preparation. A SEM image of the SWCNT fiber cross-section cut by a focused ion beam (FIB) is shown in **Figure 11c**.
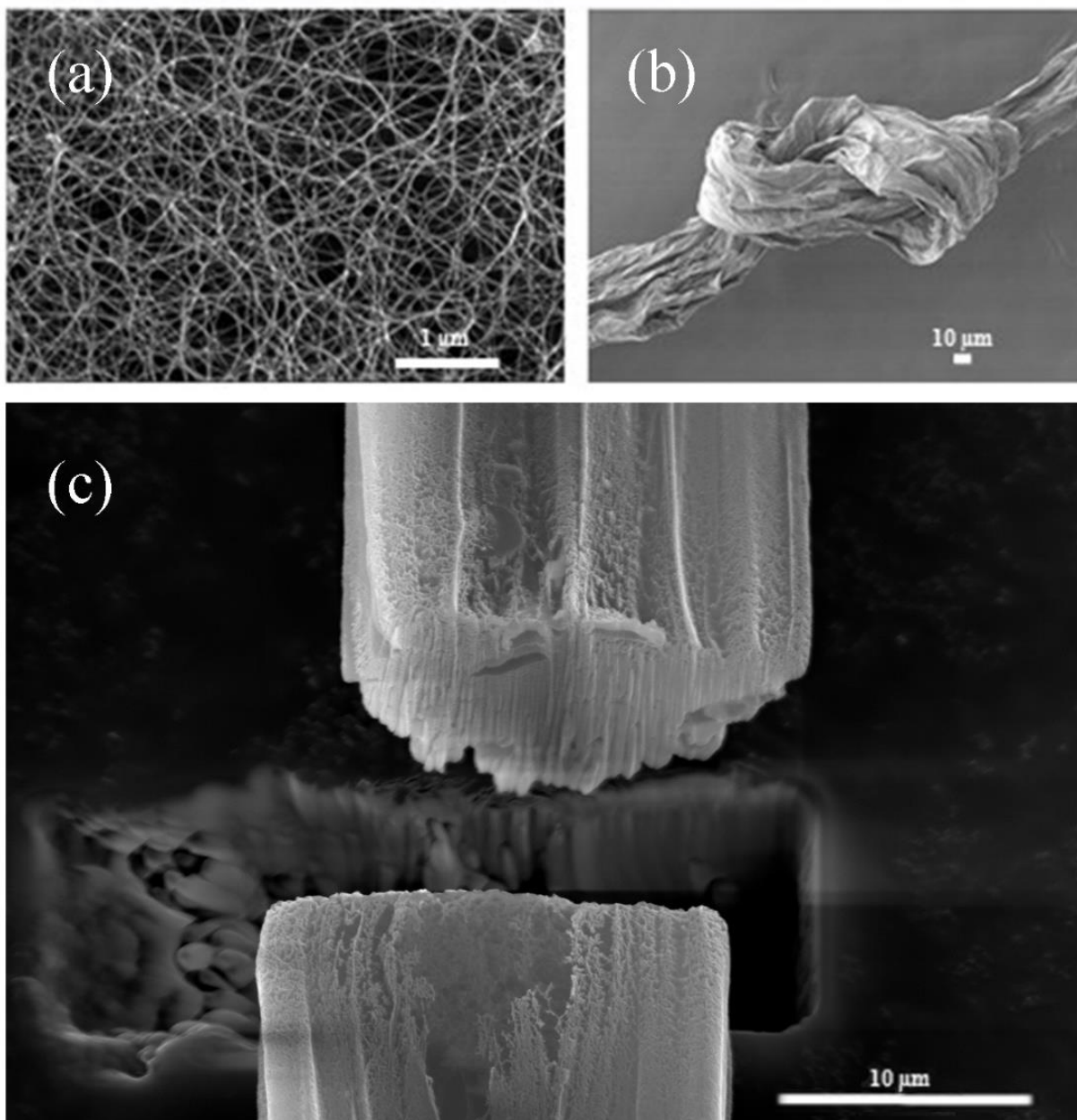
Figure 11. SEM images of (a) a pristine SWCNT film; (b) a SWCNT fiber knot; (c) a SWCNT fiber cross-section after FIB cut.

The quality of the SWCNTs, which can be estimated on the basis of Raman measurements, was found not to have any significant changes after the fiber fabrication. The intensity ratio of G to D peaks in both cases was about 100. Raman spectra of the SWCNT film and fiber made from the same film are shown in **Figure12**.
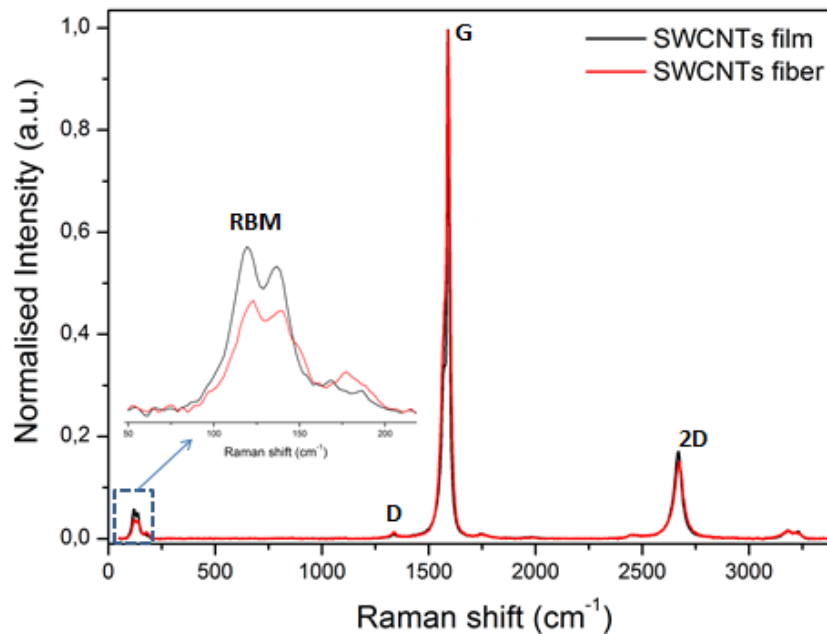
Figure 12. Raman spectra of the SWCNTs before and after the fiber fabrication.

3.2.2. Mechanical and electrical properties

Varying initial thickness of the CNT films results in fibers with different geometrical and therefore physical parameters. The dependences of the fiber diameters on the film thickness and width are illustrated in **Figure 13a**, where we obtained fibers with a diameter ranging from 41 to 140 μm. The resulted fiber diameters show the linear correlation with the initial SWCNT film thickness **Figure 13a** (II) with the R-squared parameter equals 0.93.

Apparently, the strength and resistance of the fibers depend on their diameters. Mechanical properties of the fabricated SWCNT fibers were studied in tensile, fatigue and three-point bending devices. During these mechanical tests, we also recorded the electrical resistance of the fibers. **Figure 13b** shows the simultaneous tensile tests and 2-wire resistance measurements of SWCNT fibers. The tensile curve demonstrated short elastic (1.2% strain) and then plastic behavior. The last one is caused by displacement and rearrangement of the CNTs within the fiber. Fibers, made of thinner

films, experience larger changes in the resistance during the stretching process. There is a small fibrillation due to the layer separation during the fiber break (see the chapter 3.2.3.). As can be seen from **Figure 13b** the thinner CNT films show lower Young's modulus values; this can be partly explained as the consequence of the structure heterogeneity of thinner CNT films. In addition, a thinner film has a larger fraction of CNTs located on the film surface, surrounded by fewer CNTs, thereby resulting in weaker adhesion between film constituent elements and subsequently in less strength [72].
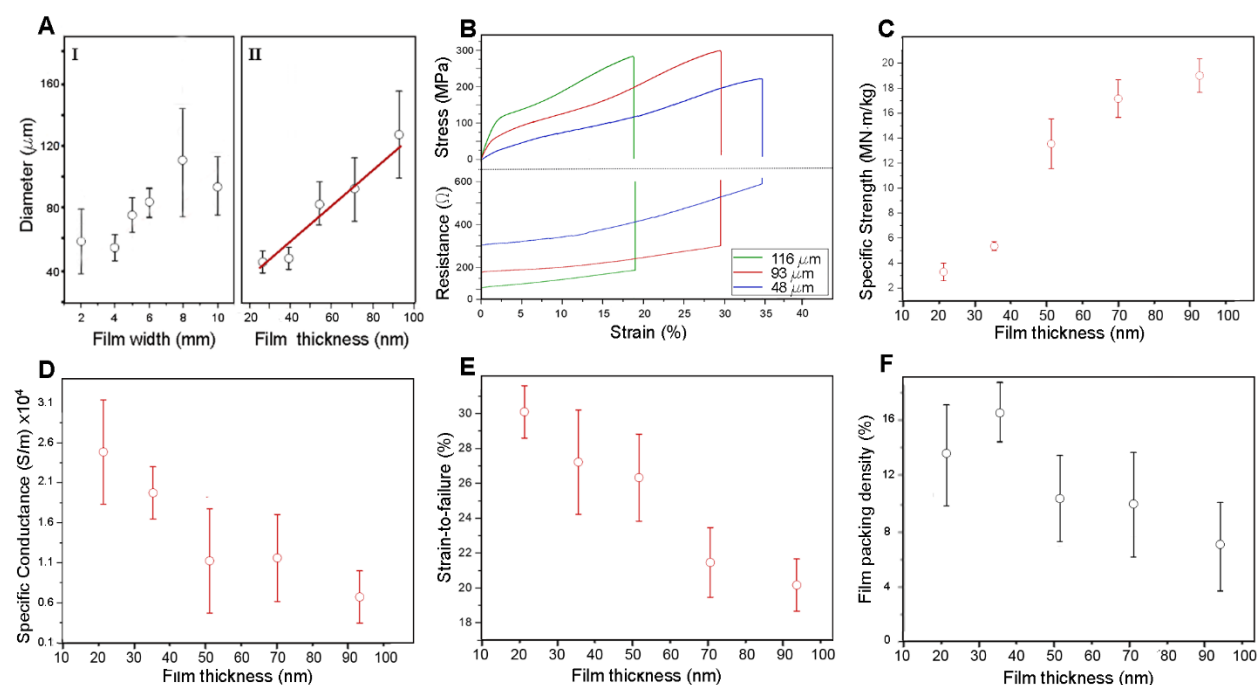
Figure 13. WP produced SWCNT fiber properties. (a) Dependence of the fiber diameter on (I) width and (II) thickness of initial SWCNT film. (b) The stress-strain plot and simultaneously measured resistance for different fibers. (c) The specific strength of the SWCNT fibers, made of different thickness films. (d) The specific conductance of the SWCNT fibers made of different thickness films. (e) The strain of the SWCNT fibers made of different thickness films. (f) Film packing density in fibers, made of different thickness films.

Plots in **Figure 13** shows how the desired characteristics can be controlled. **Figure 13c**, **Figure 13d** and **Figure 13e** illustrate the linear dependences of specific mechanical and electrical fiber properties on the initial film thicknesses. Thus, according to the application considered and specification, one can vary the initial thickness of the SWCNT film. As you can see from Figure 13E the strain-to failure is greater for the thinner fibers. Thus it would be beneficial to use thinner fibers to detect/measure displacements. Thicker fibers would be better for high sensitivity, low bending applications, for example, nanophones. The WP produced 1cm fibers possess good strength, from 300 to 700 MPa, as well as low electrical resistivity, from 60 to 300 Ohm, which is competitive to the other previously reported CNT fibers, especially from randomly oriented CNTs [21,69,73,74]. Clearly, our technique of the WP fiber manufacturing applied for aligned CNTs might improve these parameters, as well as post-treatment, e.g. twisting, doping, stretching, etc. [75–81]. On the other hand, random CNT network opens broader opportunities for force/deformation sensing applications.Error bars in Figures 12A, C, D, E, and F demonstrate the repeatability of the fibers' characteristics relative to the initial film parameter. It is worth noting that all presented fibers were produced manually. There are obvious factors, e.g. natural handshaking, speed, and angle variation while hand pulling, which affect repeatability drastically, due to manual operation. No doubt during industrial fiber manufacturing, where all these procedures would be automated, the repeatability factor would significantly decrease."

One of the main parameters which determine the mechanical and electrical properties of fibers is the cohesion of its constituent segments [2], which in turn depends on the packing density. The dependence of the packing density, defined as the ratio of the cross-sectional areas of the film and fiber, on the film thickness is presented in **Figure 13f**. As can be seen, the value of the film packing density in the fiber is relatively low and tends to decrease with increasing the film thickness. In order to define the major parameters controlling the film packing density, we analyze the process of self-assembly of the wetted film into a fiber. According to the film folding model (see chapter 3.1.4), the minimum curvature diameter, *l*, at the bending points of the film, is

determined by an equilibrium of the surface tension forces and the elastic forces of the film:

$$l = (E/12\sigma)^{1/2}a^{3/2}. \tag{16}$$

Here, E is the elastic modulus of the film, σ is the coefficient of the surface tension of the liquid (ethanol), and a is the thickness of the film. Within the framework of this model, a part of film layers are stacked together in the form of a loop (an elastic model [82]) due to van der Waals interaction (see chapter 3.1.4). The packing density is greater with a smaller radius of the loops, *i.e.,* at a smaller film thickness, which is in agreement with the experimental data (see **Figure 13f**).

3.2.3. Breakage of a fiber

A step by step SEM images of the fiber breaking process is shown in **Figure 14**. It is clearly seen that there is small fibrillation due to the layer separation before the break.

Figure 14 demonstrates the deformation-induced changes of the as-produced fiber during its elongation. It is clearly seen that there is a small fibrillation due to the rupture and exfoliation of CNT layers (folds of the CNT film) on the fiber surface.
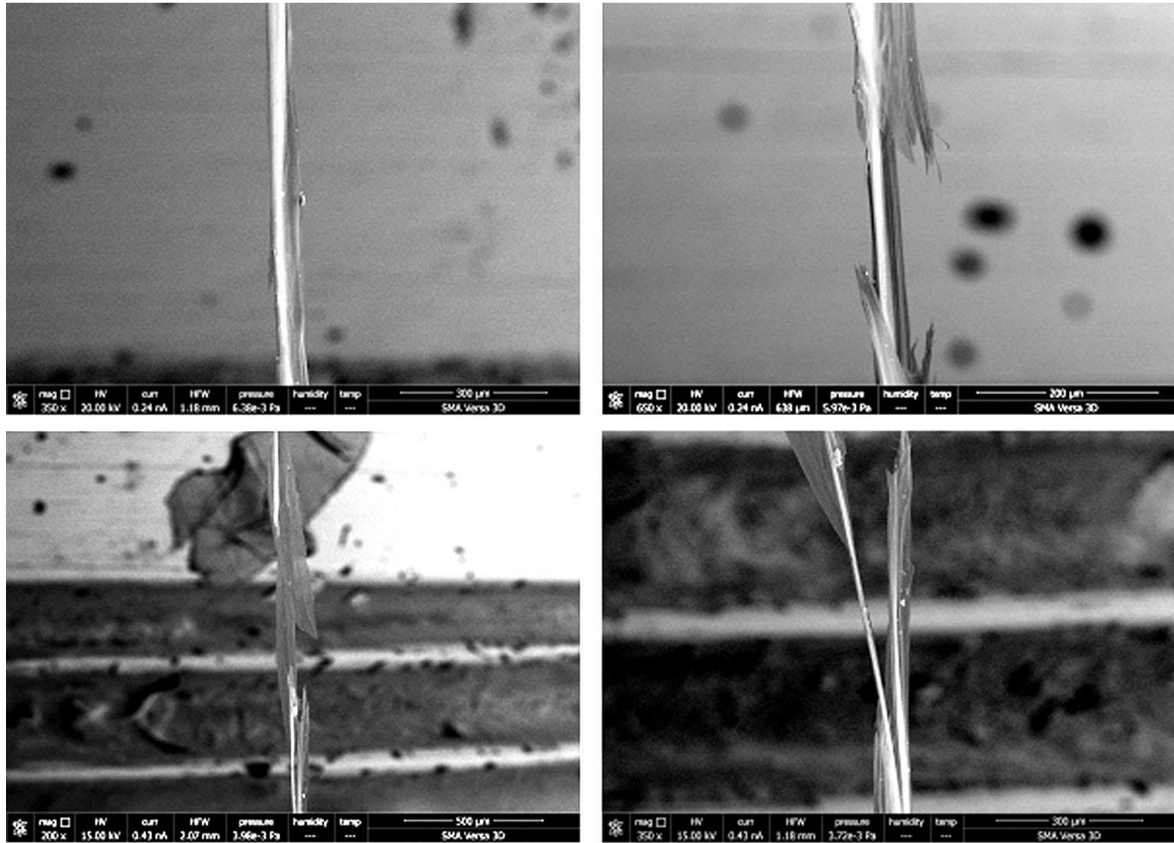
Figure 14. *In situ* SEM images of the fiber under deformation.

3.3. WP fiber properties' enhancements

3.3.1. PDMS encapsulation

Many applications (sensors, stretchable and flexible electronics, smart textile, flack jackets, etc.) restrict direct physical contact of fibers with other device elements or skin. In this work, SWCNT fibers were encapsulated with PDMS for protection purposes. A brief description of the encapsulation procedure is the following. Firstly, a thin PDMS film was prepared, a silicone elastomer base and a curing agent (184, SYLGARD®) were mixed with a ratio of 10:1 respectively and poured on a glass petri dish (resulted film thickness roughly 500 microns) with the subsequent heating (90°C for 20 minutes). After complete curing, a rectangular strip of PDMS was cut (size of 5 x 15 millimeters)

with a razor (**Figure 15a**). Then, copper self-adhere tape contacts were attached to both ends of the strip (**Figure 15b**). Further, the WP produced SWCNT fiber was immersed in ethanol and put on a strip with copper contacts (wet fiber contact results in a good adhesion). To ensure electrical contact and enhance mechanical stability, the fiber was glued to copper contacts with a little amount of conductive epoxy (CircuitWorks® Conductive Epoxy, Product #CW2400) (**Figure 15c**). Next, the fiber was covered with a liquid PDMS layer and subsequently cured on a hotplate. As a result, PDMS encapsulated SWCNT fiber is prepared (**Figure 15d**).

(a)   (b)   (c)   (d)

Figure 15. PDMS encapsulation process of the SWCNTs fiber. (a) A thin layer of PDMS is prepared. (b) Copper self-adhere tape is attached to the PDMS. (c) A SWCNT fiber is glued with silver conductive paste. (d) It is covered with liquid PDMS, then cured. In addition, wires are soldered to the copper tape.

Lower or higher force bounds for detection depend largely on the modulus of the sensing element as was mentioned above. While the sensing fiber may be capable of lower force limits depending on the thickness of the PDMS encapsulation. However, the thinner layer of PDMS encapsulation would allow for a measure of low loads and susceptibility to failure due to the strain limits of the fiber. A thin PDMS layer will also reduce the force sensing reliability of the WP SWCNT fiber to higher loading conditions, thereby limiting the wide force range capability of the force sensor. Such tradeoff is usually evidence in sensor design based on materials characteristics. A sufficient PDMS cover of about 4 mm has shown optimal reliability to our proposed force sensor designs what is tested in a preliminary experiment.

3.3.2. Solvent selection, doping, twisting

Typical morphology of the WP-produced fibers is illustrated in **Figure 12c** where one can see the folds formed during the pulling of a wetted SWCNT film. Note that a large number of the folds on the fiber surface is a unique feature of the WP method. These lead to a substantial increase in the fiber surface area, which is advantageous, for example, for gas-sensing applications or supercapacitors.

The bulk densities of the as-produced fibers were found to be 0.027–0.085 g/cm^3, corresponding to the packing degrees of 0.023–0.071. Application of twist (**Figure 16**) results in a fiber compactification and increases the packing degree up to ~0.15.

In **Figure 16,** there are optical microscope photographs of the regular (**Figure 16a**), twisted (**Figure 16b**), and coiled fibers (**Figure 16c**). It is clearly seen the difference and wavy structure. Even after twisting, our fibers remain among the least dense CNT fibers considered in the literature. Despite their low density, the specific strength and conductivity are relatively high, as discussed later, thus indicating a good interconnection of the CNT bundles. The twisting process is accompanied by a smoothing of the fiber but does not lead to the complete disappearance of the folds. This means that the CNT sliding in the folds is limited by the internal friction forces and the folds are stable structural elements of the manufactured fibers.
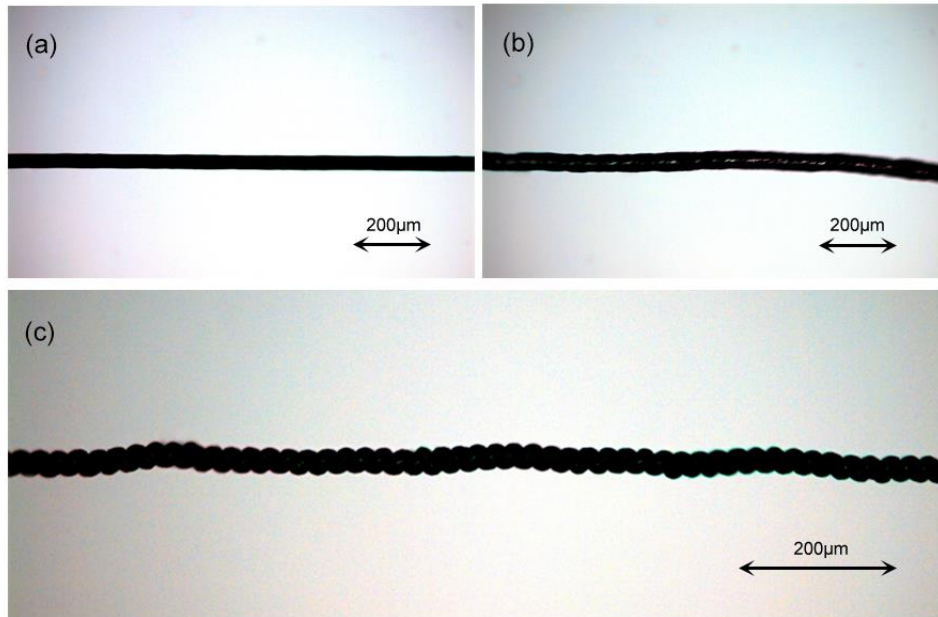
Figure 16. Microscope photograph of the (a) regular, (b) twisted, and (c) coiled WP SWCNT fiber.

Electrical characterization.

Figure 17 shows the dependence of the fiber electrical conductivity on the packing degree. As can be seen from **Figure 17**, the use of various wetting liquids leads to the formation of fibers with different properties. Fibers formed using ethanol demonstrate the lowest packing degree (f = 0.023) and correspondingly low conductivity (100–150 S/cm). Similar results on the conductivity of fibers prepared from a CNT film with 60% transparency were obtained with ethanol experiments.[33] As a result, among DMSP, THF, acetone and ethanol, it follows that DMSO and acetone give fibers with notably higher packing degree and conductivity compared to those obtained with ethanol, whereas THF is found to produce low-density fibers with the largest resistivity. The observed increase in conductivity when going from ethanol to DMSO and acetone is due to an increase in the fiber density as a result of the more effective CNTs' compaction. The use of acetone provides better densification of CNTs compared to other tested solvents. We attribute this to the high evaporation rate of acetone from the CNT film surface during fiber formation. Note that subsequent wetting of the fiber

in a solution with a lower evaporation rate (acetone mixed with an aqueous solution of $HAuCl_4$) leads to a decrease in the packing density (**Figure 17**). When using ethanol, which requires, in comparison with acetone, a longer time for the fiber to dry, this effect is not manifested.
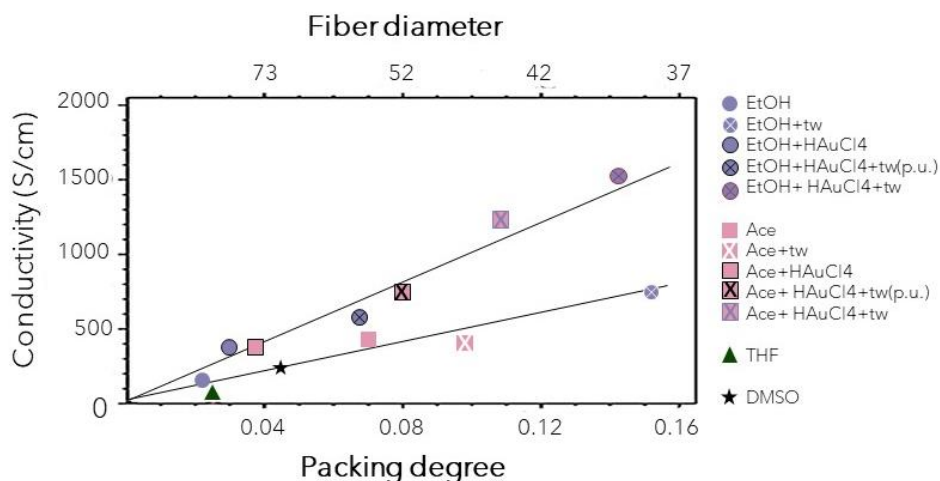
Figure 17. Dependence of the conductivity of SWCNT fibers prepared using different wetting liquids on the packing degree. The experimental data are marked by open and crossed symbols (for pristine samples) and by filled and partially filled symbols (for doped samples). EtOH – ethanol, Ace – acetone, tw – twisted fibers, tw(p.u.) – twisted and then partially untwisted fibers. The slope coefficients of the drawn lines are calculated using Equation 9 with average values of the fibers' electrical resistance.

It should be noted that our method of fiber production includes the stage of self-assembly of the wetted film when it is torn off from the substrate, which occurs in the form of multiple bends due to the action of surface tension forces. When the fiber dries, due to the evaporation and desorption of liquid molecules from the CNT surface, film sections stick together in many local places of folds (through intertube interaction), which will prevent them from straightening after complete solvent evaporation. The high volatility of acetone can increase the number of local contacts of the film[27] and, accordingly, lead to a denser packing of the fiber than in the case of DMSO evaporation.

The largest average value of conductivity for undoped fibers, ~730 S/cm, is achieved after applying a twisting process. The conductivities of some individual undoped samples have reached ~1000 S/cm. These values are comparable to the best data for fibers fabricated via dry spinning from a CNT forest, but in most cases are inferior to the reported conductivities of fibers directly drawn from a CVD reactor.[83–86] As for the high electrical performance of wet-spun fibers, their higher conductivity can be largely linked with the treatment in strong acids, like chlorosulfonic or sulfuric acid, leading to functionalization of CNTs as discussed in the literature.[86] In some studies, the acid treatment is combined with special mechanical processing to enhance the material's properties. Thus, the conductivity of strengthened CNT fibers, obtained in a recent work[87] after the drawing processing and acid treatment reached 7.6·103 S/cm, and the specific electrical conductivity (the conductivity divided by the corresponding CNT fiber density) was found to be 720 $S·m^2/kg$. Note that the specific conductivity is free from the influence of the sample volume. In our case, the best average value of the conductivity ($\sigma_e \approx 1.53·103$ S/cm) of the obtained twisted and doped fibers with a low density ($\rho = 170$ kg/m^3, f = 0.14) correspond to a specific conductivity of ~ 900 $S·m^2/kg$, which exceeds the value reported for strengthened fibers in Ref. [87]

Some of the twisted samples underwent processing in a solution of $HAuCl_4$ with loose fiber ends, which led to partial untwisting accompanied by a decrease in the packing density. The data for such samples were processed separately, their designations in the legend of **Figure 17** terminate with "(p.u.)". Partially untwisted fibers degraded in conductivity but were useful in establishing the general character of the σ_e dependence on the packing degree.

As seen from **Figure 17**, the measured conductivities are well described by a linear dependence on the packing degree. The slope coefficients of the lines shown in **Figure 17** for undoped and doped samples have been derived from the average values of their electrical resistance. The linear dependence of the conductivity corresponds to the propensity of maintaining the fiber resistance regardless of the type of wetting liquid utilized for the fiber formation and the amount of twisting. Indeed, according to

44

Equations (9), (12) and (14), the dependence of conductivity σ_e on the fiber packing degree f can be represented as

$$\sigma_e = k \cdot f \,,\tag{17}$$

where

$$k = \rho_{max} L^2 /(mR) \,.\tag{18}$$

Therefore, if the sample resistance is independent of the preparation procedure, R = const, then for a given fiber mass and length we get k = const. Note that all fibers were formed from the fragments of CNT film with fixed longitudinal and transverse dimensions, which contain approximately the same number of tubes. In a smaller diameter fiber, the number of intertube contacts is higher. This leads to an increase in conductivity so that the product of σ_e and S in Equation (9) tends to be nearly constant in the studied range of packing degrees.

The average R values and measurement errors (with a confidence level of 0.9) for fibers obtained using different liquids are listed in **Table 1**. Averaging was carried out over all samples prepared with a given liquid, including the twisted ones. As seen, the fibers under study can be arranged into three groups by the value of R. Undoped specimens have the same resistance (~120 Ohms) within the measurement error range, with the exception of fibers formed with THF. In the latter case, the average R value is significantly higher (~320 Ohms). $HAuCl_4$-doping of CNTs leads to a decrease in resistance by about a factor of 2 (from ~120 to ~60 Ohms). It should be noted that the use of a solution of $HAuCl_4$ in ethanol or acetone directly in the process of fiber formation or in the subsequent processing of an already fabricated fiber had almost the same effect on the sample resistance. Indeed, when utilizing the first approach we obtained the samples with R = 54 ± 4 Ohm, while the second one resulted in R = 57 ± 4 Ohm. It can be concluded that 1-min processing time is sufficient for the $HAuCl_4$ solution to penetrate into the fiber volume, probably due to fiber porosity and capillary effect.

Table 1. Average electrical resistance R of the fibers 1 cm long fabricated by the WP technique using different solutions.

Liquid	Ethanol	Ethanol + HAuCl$_4$	Acetone	Acetone + HAuCl$_4$	DMSO	THF
R, Ohm	120±24	55±7	118±14	65±10	123±16	320±47

The higher electrical resistance of the samples prepared with THF can be related to a deterioration of the intertube (inter bundle) conductivity in the presence of THF molecules between nanotubes, which is confirmed by FT-IR analysis (see the discussion below). This effect was not observed when using other liquids; therefore, when determining the proportionality coefficient of the linear dependence $\sigma_e = k\,f$, the data for THF were excluded. Taking the average values of 120 and 59 Ohms for the resistance of pristine and doped fibers, respectively, we calculated the corresponding slope coefficients k of the lines shown in **Figure 17** to be $5.0 \cdot 10^3$ and $1.0 \cdot 10^4$ S/cm. The derived k values determine the conductivity limits for densely packed undoped and HAuCl$_4$-doped SWCNT fibers consisting of tubes with a diameter of ~2 nm. The conductivity limits will increase with the use of thinner SWCNTs of close diameters when the maximum bundle density increases (see Eq. (15)).

It should be noted that, because of using randomly oriented SWCNT networks for fiber production, the obtained theoretical limits take into account the rise in conductivity mainly due to an increase in the material density. On the other hand, the high packing degree, close to 1, is possible only in fiber with aligned CNTs. Indeed, we can get the maximum value of f = 1 only in fiber with perfect hexagonal packing of CNTs. The effect of CNT ordering can significantly increase the real conductivity limits.

Mechanical properties. Next, we examined the mechanical properties of the samples by a tensile test. Based on the measurements of the tensile force as a function of the fiber elongation, the strain dependences of the specific energy absorption E$_s$ were calculated. As seen from **Figure 18**, the specific energy absorption increases non-

linearly with deformation. The fracture strains are found to be in the range of 7.5–23%. On the whole, the response of a CNT fiber on the applied stress is determined by van der Waals forces. However, CNT fibers have a complex hierarchical organization of structural components, which makes it difficult to analyze the evolution of a material under mechanical load. There are three levels of elements' organization that increase in complexity – from individual nanotubes with different chiralities and lengths at the lowest level, to CNT bundles, which form an entangled network. These levels resemble a biomaterial hierarchy, as noted in Ref.[88]
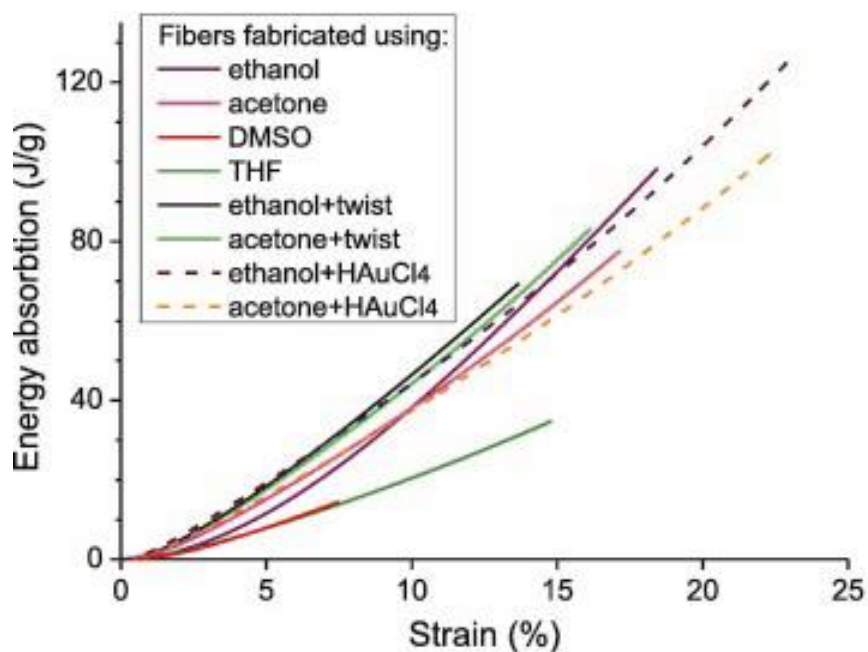
Figure 18. Strain dependence of the specific energy absorption for fibers prepared using various solutions, without and with the subsequent processing.

Energy absorption at the initial stage of loading is due to the elastic deformation of CNT bundles followed by overcoming the van der Waals forces and sliding motion of the CNTs. The latter occurs when the shear stress on the interfaces between the CNTs exceeds a certain threshold value determined by the weakest intertube contact. Therefore, the contact area between the tubes is a key factor that defines the load-bearing capacity of the fiber. The sliding friction strongly affects load transfer and stress distribution in a CNT assembly and can be increased in collapsed CNTs.[89] It is obvious

that CNTs in fibers with low packing densities will experience slippage under stress to a greater extent, which explains the high strain values we have obtained. A ductile failure mode due to a CNT pull-out is evident. A closer inspection of the deformation behavior of the as-prepared fibers has shown small fibrillation due to the rupture and exfoliation of CNT layers (folds of the CNT film) on the fiber surface (**Figure 14**). The fibrillation can be eliminated by strengthening the surface of the fiber by a thin metal coating (**Figure 16**).

As follows from the results obtained, the ability to absorb mechanical energy under deformation is significantly dependent on the preparation and post-processing conditions. The fibers formed with DMSO and THF have demonstrated the lowest values of total absorbed energy up to fracture (toughness) of 15–35 J/g. The highest values of toughness were achieved for fibers treated in the solutions of $HAuCl_4$ in ethanol (127 J/g at 23% strain) and acetone (103 J/g at 22% strain).

The representative mechanical and electrical properties of the WP-produced fibers are presented in **Table 2**. The tensile properties listed in **Table 2** were determined as a result of single measurements for each sample with a relatively small instrumental error. The elastic modulus was derived from the initial slope of the engineering stress-strain curve. After twisting, the fibers became thinner and more uniform in diameter along their length. Interestingly, the specific strength is found to be only weakly dependent on the sample fabrication conditions. The obtained tenacity values of 0.60–0.78 N/tex are close to or even exceed the published data for fibers directly spun from a CVD reactor using a bath-spinning method (0.4 N/tex[87] and 0.2–0.75 N/tex[90]) and a rotating-anchor spinning method (0.4–0.6 N/tex for a 8 mm gauge length,[91] 0.44–0.65 N/tex,[92] and 0.84 N/tex[93]). In addition, our best samples show notably higher toughness, which outperforms that of Kevlar (78 J/g). This is due to a combination of low density with an ability of WP-prepared fibers to sustain large deformations, up to 23%, whereas most neat CNT fibers discussed in the literature exhibited fracture strain of 1–10%.[31,32,85,94,95]

The low density of the obtained materials is attributed to the presence of voids inside the fiber due to the formation of loops during the folding of CNT network.The comparison of the measurement results shows a tendency for the density of the fibers fabricated using acetone to decrease after the treatment in the $HAuCl_4$ solution. The density decrease means the decrease in the packing degree of CNTs. We attribute this effect to a relaxation of internal mechanical stresses after the fiber wetting in the solution with a lower evaporation rate (acetone mixed with an aqueous solution of $HAuCl_4$).

Twisting reduces pores within the fiber structure. The fiber stretching also has a similar effect, which leads to a fast reduction in diameter at a small tensile strain (**Figure 16**) that results in the high Poisson's ratio of 7 at $\varepsilon = 4\%$. As seen from **Table 2**, the density of the twisted fiber is up to ~7 times higher than that of the untwisted sample. Accordingly, the contribution of the CNT bundles' elastic properties to those of the fiber increases, and the elastic modulus shows a significant improvement. However, the fracture strain of the twisted fiber is reduced in comparison with the untwisted sample. Thus, the difference between the fracture strains for fibers produced with ethanol amounts to 5% (**Table 2**); in this case, the substantial reduction of strain at failure in combination with the increased density does not allow to obtain higher toughness compared to the untwisted fiber. On the other hand, the twisted fiber exhibits an enhancement in the absorption energy at small deformations (**Figure 18**).

Table 2. Mechanical and electrical properties of the fibers with the best specific conductivity among the samples formed under given conditions. d is a diameter, ρ is a density, ε_f is a strain-to-failure, T_s specific tensile strength, ε_e specific elastic modulus, C_s specific conductivity of a fiber.

Fabrication conditions	d, μm	ρ, kg/m^3	ε_f, %	T_s, N/tex	ε_e, N/tex	C_s, kS·m^2/kg
Ethanol	97 ± 13	27 ± 5	18.4	0.78	10.9	0.64
Ethanol + twist (50 turns/cm)	37 ± 3	186 ± 21	13.4	0.64	32.8	0.45
Ethanol + HAuCl$_4$	99 ± 14	26 ± 4	23.0	0.69	39.2	1.19
Acetone	57 ± 7	80 ± 14	17.3	0.62	24.6	0.50
Acetone + twist (30 turns/cm)	51 ± 5	93 ± 13	16.1	0.70	36.8	0.46
Acetone + HAuCl$_4$	68 ± 9	56 ± 10	22.4	0.60	35.4	0.93

Improving the mechanical properties of CNT fibers expands the possibilities of their use in materials and devices operating in harsh service conditions. Different chemical and mechanical treatments can be applied to tailor the fiber characteristics. Note that fiber twisting is an optional post-processing procedure in the WP technique compared to the methods where twisting is inextricably linked to the process of fiber formation. This means that various fiber processing methods can be freely used in different combinations, thus making it possible to choose the most suitable sequence of thermal, chemical and mechanical treatments to obtain a material with desired properties.

Resistance response to strain. For stretchable electrically conductive materials, the sensitivity of electrical resistance to the strain magnitude, which is determined by GF, is very important. The GF value should be high enough in materials being developed for sensor applications, or very low if a stable behavior of a conductor is required independent of deformation. The dependences of the relative change in electrical resistance and GF on the strain for the as-produced (untwisted), doped and twisted fibers are plotted in **Figure 19**.
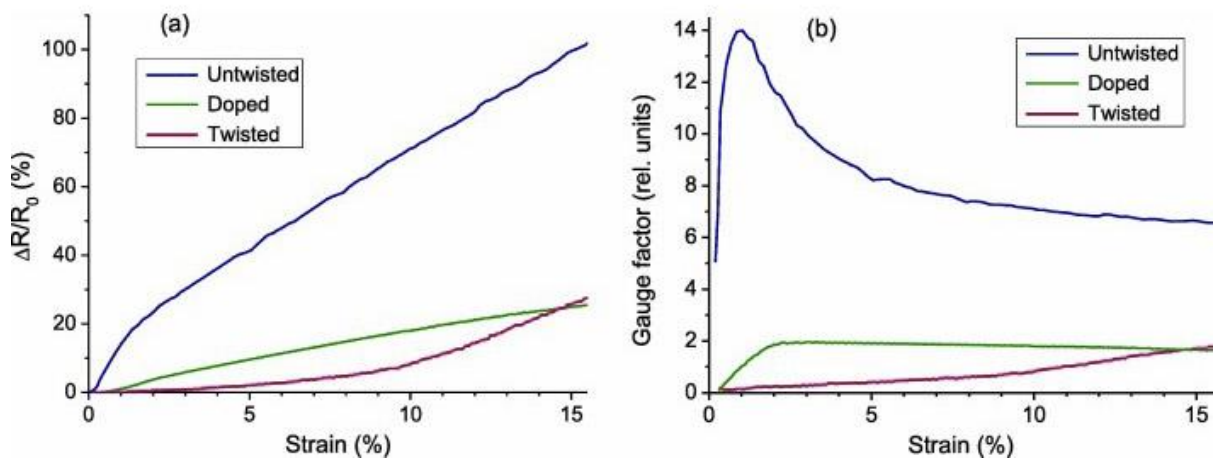
Figure 19. Strain dependence of (a) the relative change in resistance and (b) the GF for the untwisted, doped (without application of twist), and twisted fibers produced using acetone.

As can be seen from **Figure 19a**, $\Delta R/R_0$ monotonically increases with the fiber tension. GF is the ratio of a relative change in the fiber electrical resistance, $\Delta R/R0$, to the corresponding mechanical strain, ε: $GF = (\Delta R / R_0)/\varepsilon$. Thus the obtained $\Delta R/R_0$ values for the twisted fiber correspond to a GF of 0.2–0.4 in the strain range up to 4%, which is in line with literature data for fibers drawn from a CNT array.[77,96] The as-prepared untwisted fiber exhibits a pronounced non-linear behavior at strains up to 3%. The slope of the $\Delta R/R_0$ curve in this range noticeably changes, which leads to the appearance of a peak on the GF curve (**Figure 19b**). The GF of the untwisted fiber rapidly increases to a maximum of 14 at 1% strain and then more gradually decreases to a limit of 6.6. The high sensitivity of the untwisted CNT fiber in the range up to 1% is favorable for the creation of small-displacement sensors.

3.4. Applications

3.4.1. Force sensor

Inspired by the promising functionality of the WP produced CNT fibers, we then demonstrated its practical applications in the form of active and passive electronic components. To unveil the performance of the SWCNT fibers, the force sensor was designed and investigated (**Figure 20).**
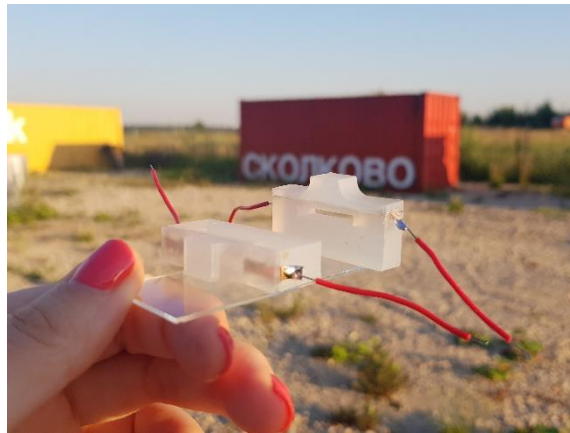
Figure 20. Basic design of the semitransparent sensor architecture.

Force sensor fabrication. The force sensor consists of three major elements: the base, the sensitive part, and the stiffener (**Figure 21d** and **Figure 21e**). We designed two similar assemblies: magnet assembly (**Figure 21d**) and screw assembly (**Figure 21e**) (see details in chapter 3.5.2).
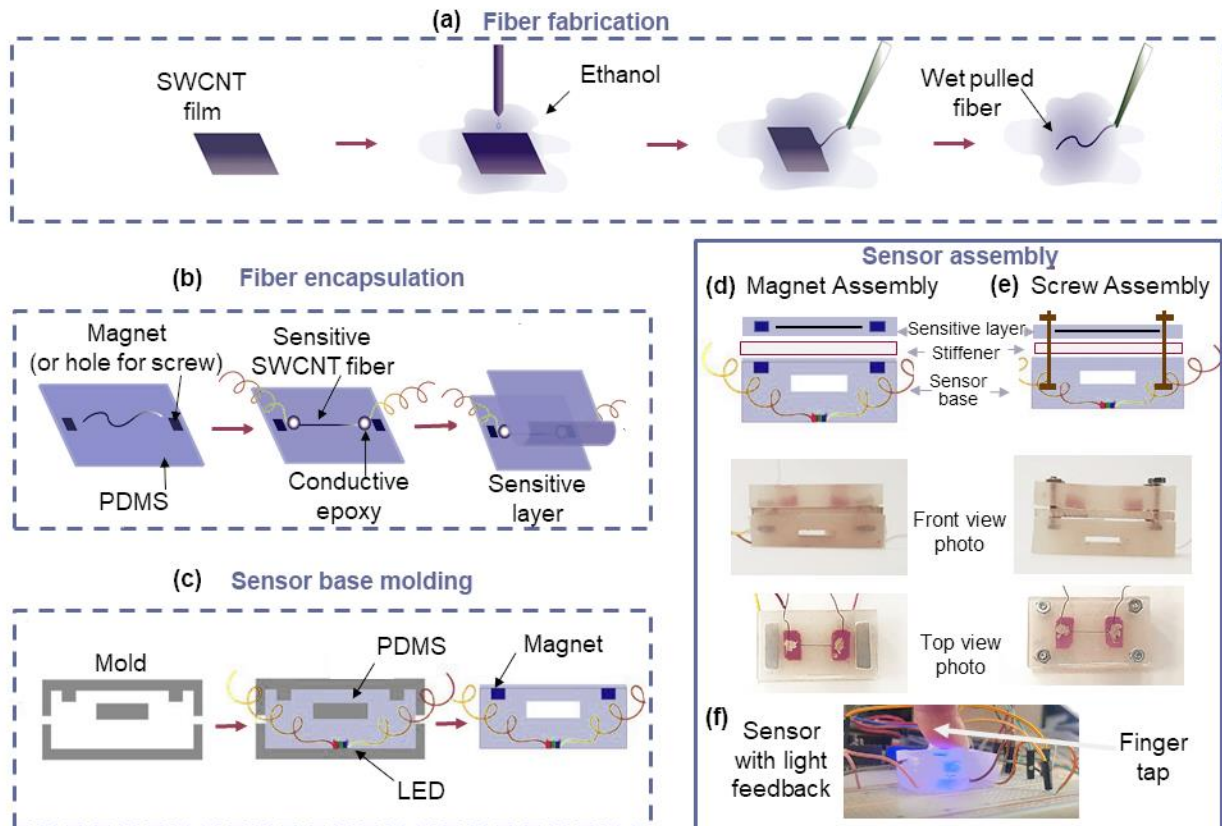
Figure 21. Sensor design and fabrication process. (a) Schematic illustration of the preparation of fiber using the WP technique. (b) Fiber encapsulation: top layer with the sensitive fiber encapsulated in PDMS procedures. (c) Molding stages for the base of the sensor. Sensor assembly with two different architectures: (d) demoldable with magnets and (e) with screws. (f) Semitransparent sensor with light feedback in operation.

As shown in **Figure 21b,** the fiber was placed on a PDMS (SYLGARD®, silicone elastomer base 184 and curing agent 184) substrate before ends of the fibers were attached to thin copper wires using CircuitWorks® conductive epoxy, Product #CW2400, which has the resistivity $<10^{-5}$ Ohm·m. Then, it was covered with PDMS to encapsulate the fiber and forms the sensitive part. The PDMS encapsulation allows for stress to be evenly distributed along the fiber's length and mechanically protects the fiber. Depending on the target application, CNT fiber may be encapsulated into other elastomers, ceramics, textiles and even composite materials. The stiffeners were made

from TPU, PLA, and Flex (very flexible polymer) (REC-3D company, Russia) 3D printer plastics (see chapter 3.5.2).

The base was cast out of the PDMS, using 3D printed molds (**Figure 21c**) (more details in chapter 3.5.1.). Light feedback LED with wires was encapsulated in the base during the manufacturing process (**Figure 26f** and video in operation link https://youtu.be/vPavrI7fCfg. The void in the base gives a space when the bending is induced under loading and unloading.

Sensor working principle. **Figure 22** shows a linearization modeling procedure utilized whereby the force sensing device is modeled as a simply supported beam (**Figure 22a** I and II). It shows the ideal force diagram during load application, w, transfer or deflection to the sensor SWCNT fiber representative element subjected to the combination of axial and shear stresses as described in **Figure 22b**(I) with the PDMS elastomer showing the typical beam sections with corresponding stresses orientation, deflection of the beam model as an equivalent mechanistic, linear spring model, $w = ky$. Where δ_{max} is the maximum deflection under loading condition at stable equilibrium and k - the equivalent stiffness of the sensor spring model in **Figure 22b**(II).

During the bending of the sensor **Figure 22a**(I), the length of the fiber increases while its cross-sectional area reduces. In similitude to a strain sensor, the resistance changes are like an ideal piezoresistive sensing material when subjected to strain. As a result, the length of the sensitive CNT fiber increases accordingly to the Poisson effect just as shearing and compression stress is induced in the sensing fiber shown as fiber representative element in **Figure 22a**(III). Hence, the total resistance of the sensor increases due to CNT displacements along the fiber axis during the bending test.
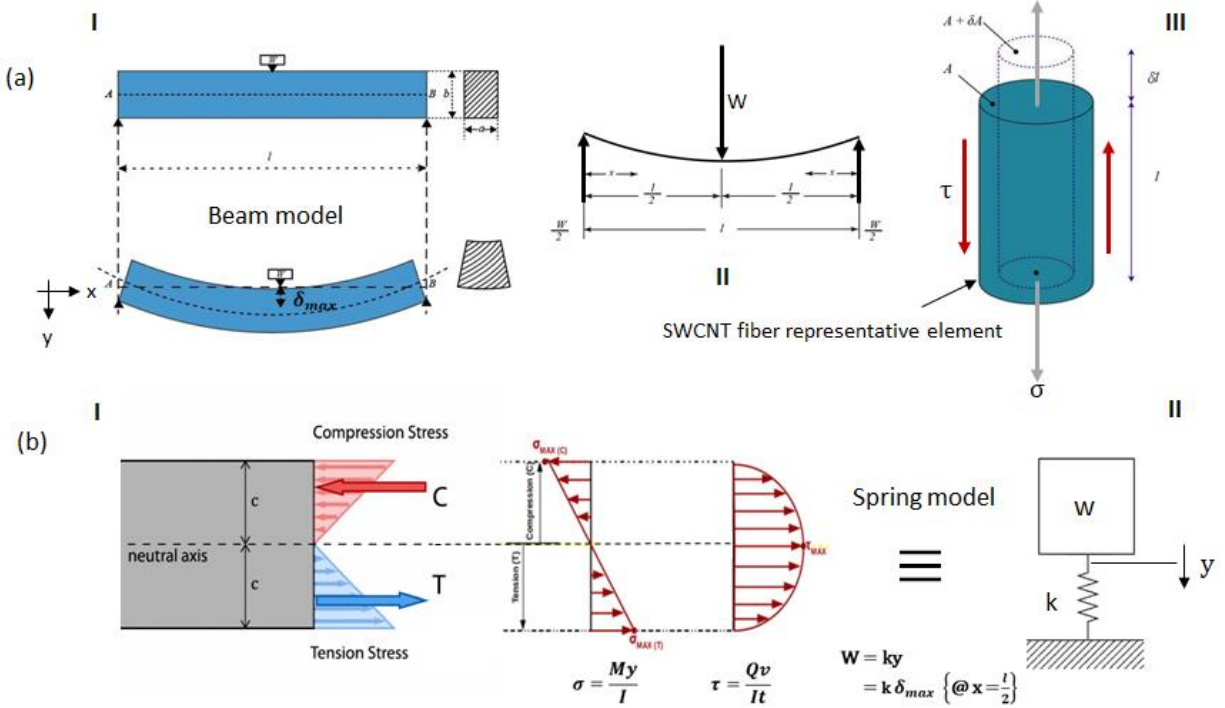
Figure 22. Sensor Mechanistic Model for Linearization. (a) Sensor model as a simply supported beam (I), the force diagram model during load, w, transfer or deflection to the sensor (II), SWCNT fiber representative element subjected to the combination of axial and shear stresses with the PDMS elastomer (III), (b) the typical beam sections with corresponding stresses orientation (I), deflection of the beam model as an equivalent mechanistic, linear spring model (W = k·y) where δ_{max} is the maximum deflection under loading condition at stable equilibrium and k is the equivalent stiffness of the sensor spring model (II).

Based on the beam model for force sensor operation, the neutral axis is located at the mid-section of the beam, where the sensitive SWCNT fiber element is positioned. The neutral axis is characterized by zero shear stresses, therefore only pure bending stress exists.

The application of mechanical stress to the sensor is accompanied by a displacement of individual CNTs with respect to each other. Hence, the consequent interaction of individual SWCNTs which different chirality, be it semiconducting or metallic, gives rise

to the characteristic Schottky barriers; appearing at regions where semiconducting tubes and metallic tubes share interfacial contacts or fibrous intersects. For a fibrous material such as carbon fibers based on CNTs, several contact domains exist in numerous regions along with the fiber. Technically, such Schottky contact domains can be modeled with resistance and capacitance in series. Therefore, a CNT fiber sensing element tends to exhibit non-linear resistive properties in response to stress-strain stimuli along its length. This gives the rationale for various studies on utilizing the piezoresistive effects as self-sensing characteristics in our sensor device fabrication.

FEM analysis of the elastomer structure (with no CNT fiber inside) was conducted to investigate the stress-strain behavior of the sensor architecture as deflection is introduced. Simulations were carried out with Solidworks® Simulation to observe the failure deflection threshold for reliable performance. The result is presented in Figure 23.

Location of SWCNT fiber
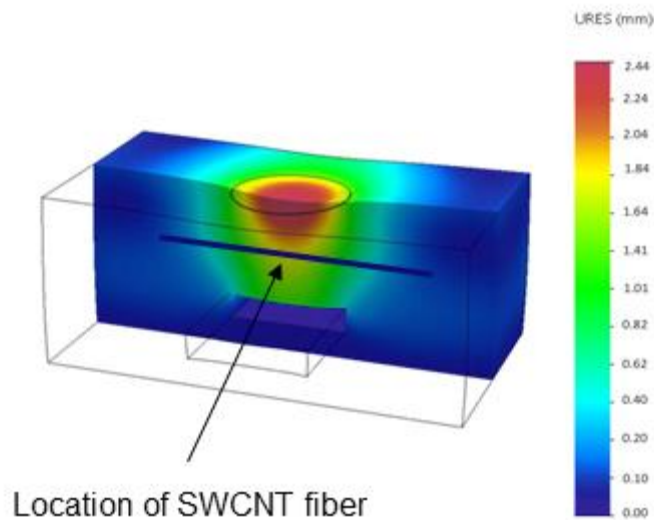
Figure 23. FEM simulation of sensor geometry with a color stress intensity gradient across its mid-section depicting the deformation due to beam-deflection controlled analysis. Location of SWCNT fiber was added to the figure after the simulation to demonstrate the fiber location inside the elastomeric structure.

In addition to the simply-supported analytical beam model, our work also presents a design procedure and deals with the implementation of the proposed concept in a functional prototype and its experimental characterization. **Figure 23** shows the FEM of the deformation propagation along with the sensor geometry when loading conditions of the simply supported beam mechanistic model are employed. The color intensity of the simulation corresponds to strain, which is characterized by the peak near the location of deflection and gradually diminishes from the deflection point. The FEM model based on the 3-point bending experiments allowed for the selection of the safe deflection limit of 2.5 mm for the sensor during operation. From **Figure 23**, at about 2.5 mm deflection impingement on the sensor, it can be identified that the ends of the fiber, represented by a superimposed black thick line, are of zero strain domains. This allowed for reliability in sensor performance, since deformation on this section leads to the destruction of SWCNT fiber – silver – copper wire electrical contacts within the PDMS encapsulation thereby leading to instability in performance.

Mechanical properties. The application of mechanical stress to the sensor is accompanied by a displacement of individual CNTs with respect to each other. Accordingly, it is expressed in changes in the fiber resistance that remain the ones of the ideal piezoresistive sensing material. The length of the CNT fiber increases accordingly to the Poisson effect just as shearing and compression stresses are induced in the fiber. Hence, a total resistance of the sensor increases due to CNT displacements along the fiber axis during the bending test.

The adjustable flexural rigidity of the sensor is attained by mounting the sensor with stiffener plates of different thicknesses, thereby varying the elastic properties of the sensor assembly. Optimization of the fiber properties may increase the sensors' sensitivity. On the other hand sensor design optimization would be more beneficial for sensing range enlargement.

The stiffener plates considered in our work offer variable stiffness (or sensor modulus) as a promising solution to outweigh the contradiction and tradeoffs between

maintaining compliance with materials' physical properties and maximizing the force sensing capacity. To determine the operating characteristics of the finger and force sensor under impinging pressure, it is necessary to choose the appropriate stiffener plates. **Figure 24a** shows the deflection input and load response for various sensor assemblies starting with the sensor without a stiffener, followed by the sensor with the selected five stiffeners. It can be described in terms of the linear spring model: tougher the stiffener, *i.e.* greater stiffness coefficient, greater load is needed to achieve the same deflection. Changing the stiffeners adapts the force range to the required one; **Figure 24b** proves the conformance of the stiffness data to the linear spring model with a linear fit (R^2 = 0.99959). The load-deflection ranges and characteristic-curve for different stiffener materials are depicted in **Figure 24c**, the stiffener increases the modulus of the sensor; "no stiffener" corresponds to the inherent stiffness of the sensor, TPU & PLA are 3D printed stiffener plates with a designated number as stiffener thickness in millimeters (mm). It is seen that the softer sensor easily deforms under the load and achieves the maximum deflection rapidly; the stiffer sensor bends a little under the load, because of the greater stiffness coefficient. Thus, taking into account the maximum sensor deflection of the exact application, one can choose the optimum stiffener, with the appropriate force range and the greater resolution. **Figure 24d** gives relative deflection variation of sensor response different stiffeners evaluated at the loading force of 10 N, which thereby validates that increasing modulus of the sensor allows for adjustable force sensing.
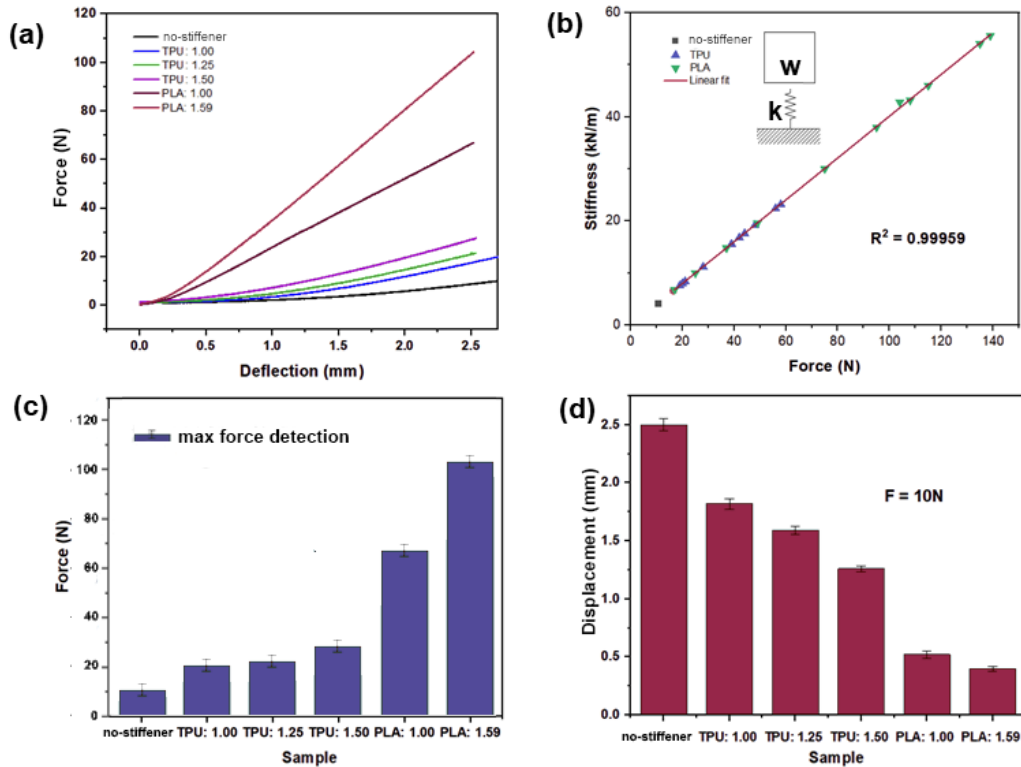
Figure 24. Mechanical properties of the force sensor. (a) The force-deflection characteristic curve for different samples of stiffeners, which increase the modulus of the sensor; *no stiffener* corresponds to the normal stiffness of the sensor, TPU & PLA are 3D printed stiffener plates with a designated number as stiffener thickness in millimeters (mm). (b) Spring model equivalence graph with the linear fit (R^2 = 0.99959) shows conformance to the linear, mechanistic model from experimental data with stiffener made from TPU & PLA. (c) A force detection limit of the force sensor with an adjustable stiffener thickness (corresponding to increasing stiffness). (d) Displacement variation of sensor response of different stiffeners evaluated at the loading force of 10 N.

Electromechanical properties. Following the evaluation of mechanical properties, we tested corresponding electromechanical characteristics. The relative change in resistance of sensor regarding the repeated deflection of 2.5 mm for different stiffeners as a function of the applied force is presented in **Figure 25**. Individual stiffeners have different slopes and corresponding detection limits. Without the employment of the

stiffeners, the force detection range is determined to be 0 – 10 N, while with a PLA stiffener, thickness 1.59 mm, the detection range is 0 – 104 N. Various stiffener plates considered in this work offer characteristic linear curves for loading and unloading condition as provided for force measurement. Hence the sensitivity and force detection of the sensor depends largely on the selected stiffener.
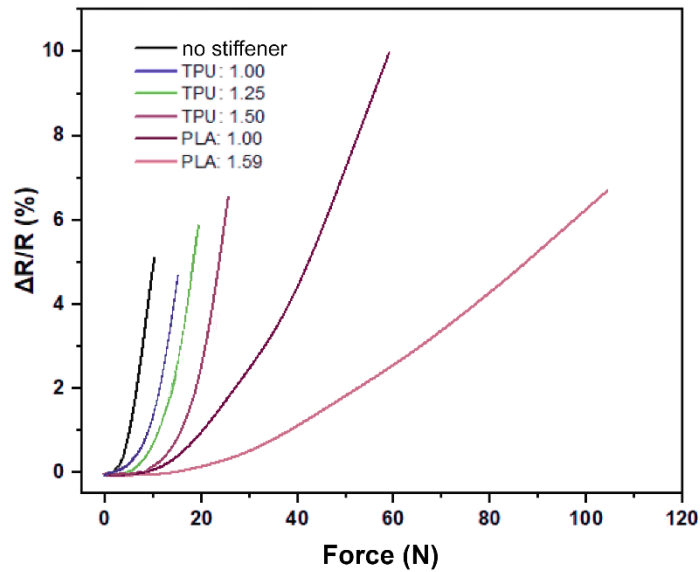
Figure 25. Relative resistance changes of the sensor with different stiffeners as a function of applied force. Number denotes the thickness in mm.

Fatigue and step load tests. Sensor training.

Fatigue test shows poor stability without training the sensors and drifts of similar delta values as the resistance changes due to a load input (**Figure 26a**). However, the training of the sensor helps to mitigate such unstable performance. The training procedure consists in applying the load to stretch the sensor for 10%, then unload, and finally applying the planned force for several times.

Figure 26b shows the output resistance plot during the fiber training used to stabilize of the sensor. After the 6th cycle the fiber possesses the stable response. Subsequent fatigue test results are shown in **Figure 26c.** A more stable response with minimal drift shows that the training is effective to achieve excellent sensor performance. During our

experiments, the same sensors were used for fatigue tests for several times and possess good stability for more than 10 000 cycles in total. The major effect of training stems from irreversible small deformations in the fiber to disappear. In this way, the true elastic deformation is achieved within the trained displacement.
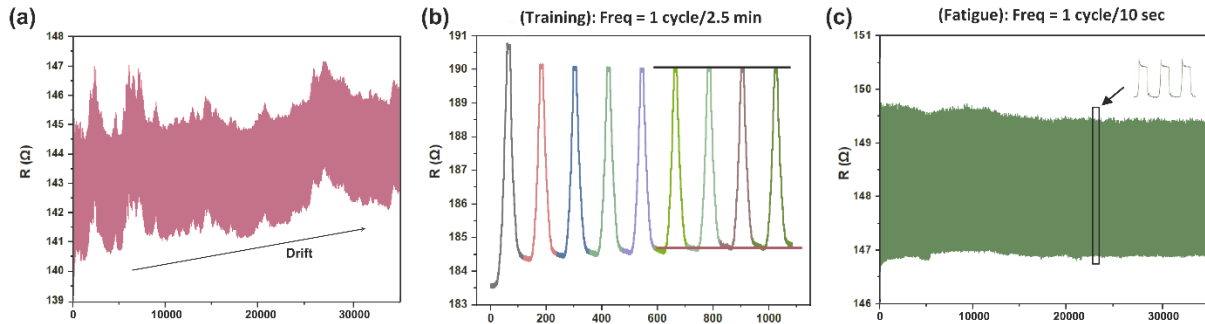
Figure 26. Effect of sensor training and step load experiment. (a) Fatigue test without training sensors shows poor stability and drifts of similar delta values as the resistance changes due to a load input. (b) Training procedure of WP SWCNT fiber. (c) Subsequent fatigue test with minimal drift and more stable response.

Also, a three-point bending test was performed to check the resistance stability of the fiber under constant load. **Figure 27a** shows measured force and fiber resistance during three cycles of stepped mechanical loads (**Figure 27b**). A slight asymmetry between load and unload resistance response is observed, which is caused by different CNT displacement mechanisms during its compression and extension. However, the resistance demonstrated a stable response to the applied loads along with the cycles. The force range depends on printed sensor body material and configuration. It can be adjustable to a wide range of forces and could be potentially used in affordable smart prosthetics or robotic grippers.
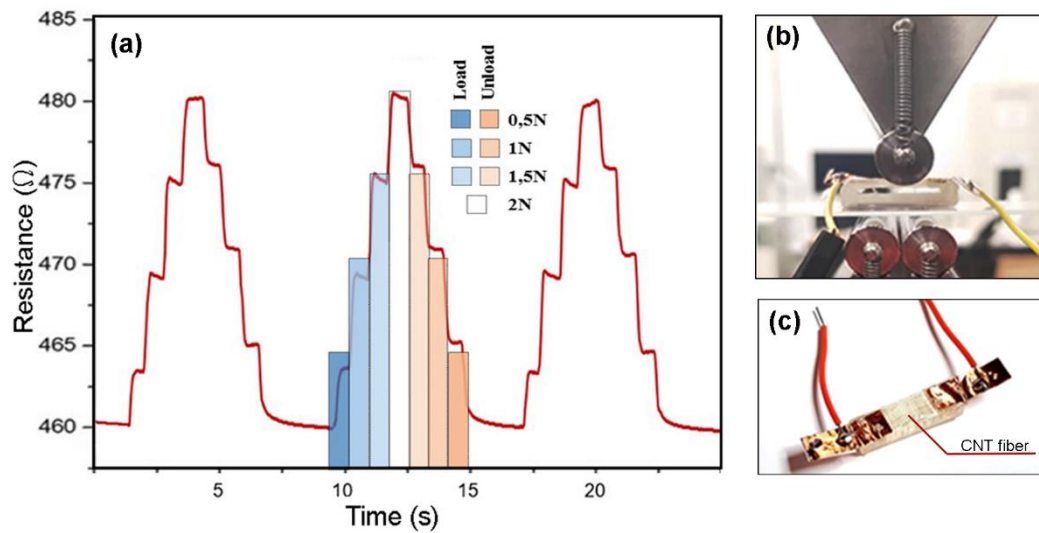
Figure 27. Step load experiment. (a) The resistance of the fiber during the three-point bending test stepped load. (b) Force sensor under tapper load (three-point bending test with wires attached). (c) A force sensor with encapsulated SWCNT fibers.

Different sensors performance

Table 3. The summary of performance of flexible strain sensors fabricated using carbon nanomaterials in the form of membrane structure, based on *Yan et.al.* [97] review.

Materials	Methods	Strain range* (%)	Gauge factor	Cycle number	Ref
SWCNT fiber	CVD and Wet pulling	8	14	10 000	This study
Single CNF	A microelectromechanical system	1.5	2.55	3	[98]
CNT fiber	CVD and twisting	500	-1.3	100	[99]
Silicone	The coaxial wet	100	0.68	10 000	[100]

rubber/MWCNT	spinning				
Graphene/PU fiber	A layer-by-layer assembly method	50	86.9	100	[101]
Carbon black/natural rubber/PU fiber	A layer-by-layer assembly method	1	43.2	10 000	[102]
CNF fiber/PU	Embedding	2	>1700	300	[103]
SWCNT wire/PDMS	Embedding	12 1.1	10 000 1	5 000	[104]
PU/Cotton/CNT fiber	Core-spun yarn	40	-	300 000	[105]
SWCNT/MWCNT/PU nanofiber	Coating	50	1.24	2 000	[106]

* Strain range here is determined according to the fatigue test for repeatability

As shown in the Table 3, WP CNT fibers possess compatible characteristics with other carbon nanomaterials-based sensors. They have a potential for a greater number of cycles (we haven't made fatigue test for more than 10 000 cycles, most probably these properties remain the same even after). Given strain range and gauge factor fit most of the applications, while simplicity of the WP technique provides it an advantage for rapid prototyping.

3.4.2. Vibration sensor

We also tested the sensor for vibration monitoring (see https://youtu.be/d_QndEFklfk). It showed a perfect response to table tap and incorporated light feedback corresponding to the amplitude of the vibration impulse (**Figure 28**).

Figure 28. Vibration monitoring system experiment. Snapshot from the experiment video.

3.4.3. Heart rate monitor

In order to demonstrate high sensitivity, encapsulated and pre-strained WP produced SWCNT fiber was attached to the neck (**Figure 29a**) and wrist (**Figure 29b**) area, then its resistance response sensitive to pulse was recorded. Using a thin pre-strained fiber helps to obtain a reasonable sensitivity, required for small mechanical displacement measurements. It is worth mentioning that in **Figure 29a** the general pattern of fiber resistance response on a pulse is combined with a periodic wavelike signal, caused by breathing. Thus, it can be used for wearable lightweight medical devices as well.
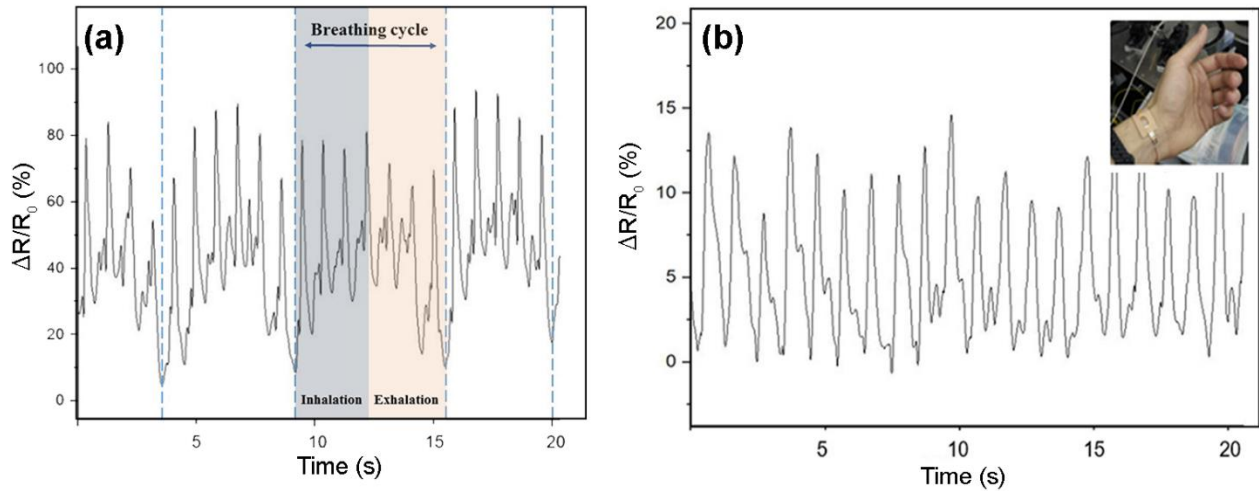
Figure 29. Heart rate monitor experiment. (a) Relative resistance change during pulse measurements on a neck is also demonstrating the possibility for breath detection. (b) Relative resistance variation during pulse measurements on a wrist.

3.4.4. Nanophone

In order to clearly show the sensitivity of the sensor to the slightest vibrations, the author has created a device capable of recording sound. It was called Nanophone. Sound sensing opportunities of the SWCNT fibers were demonstrated by recording a fragment of the Georges Bizet - "Les Toreadors" from Carmen Suite No. 1.
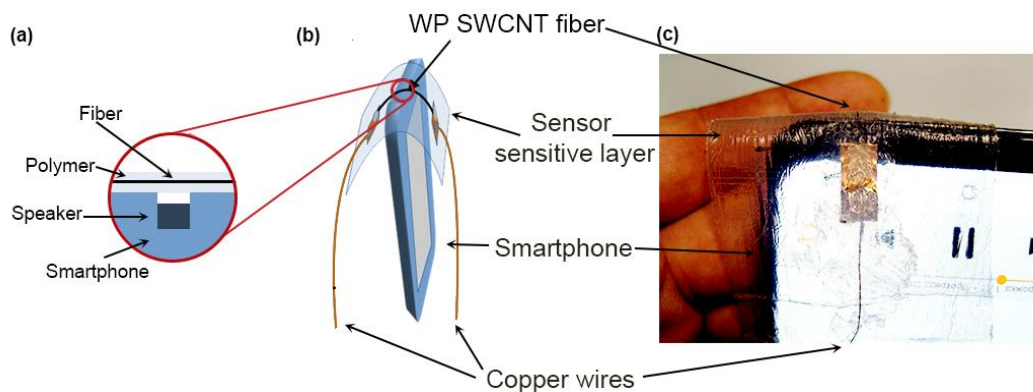
Figure 30. Acoustic experiment scheme: (a) Arrangement of the encapsulated fiber and the smartphone's speaker. (b) Pictorial setup of the experiment. (c) Image of the sensor placed at the smartphone speaker.

The experimental scheme is depicted in **Figure 30**. The sensor covers the smartphone speaker and PDMS touches the phone case. The input vibrational notes imposed an air pressure difference on the PDMS layer to serve as a membrane, which encapsulates the sensing fiber element. The membrane deformations, in turn, cause a change in the resistance of the encapsulated sensor-fiber measured during the experiments.

We have evaluated the performance of the encapsulated WP SWCNT fiber in the configuration shown in **Figure 30** in an acoustic experiment. Recorded resistance changes closely replicate the frequency domain and corresponding notes amplitude when compared to the commercially available microphone after minimal filtering. We called the device Nanophone since its core sensing elements are CNTs. See Appendix A for the audio recordings obtained for music from the sensors and microphone (with and without filtering).

Figure 37 shows the "Les Toreadors" waveform and a spectrograph of the electrical signal (resistance changes) from the sensor (Nanophone) and the standard microphone. All audio files are presented in Appendix A. The background noise obtained is due to the diaphragmatic vibration sensing architecture employed (see **Figure 31a**). After the filtering procedure, the signal resembles the signal from the microphone, which can be clearly seen in **Figure 30b** and **Figure 31c**. Such proof-of-the-concept test shows that the sensor can be used for acoustic sensing; proper filtering circuit would demonstrate a more robust opportunity for the nanophone implementation. The nanophone recordings quality is fine enough for average machine music recognition systems (we used Shazam player, Apple Inc.) to easily define the composition (see https://youtu.be/QUPqaKBdd5Y).
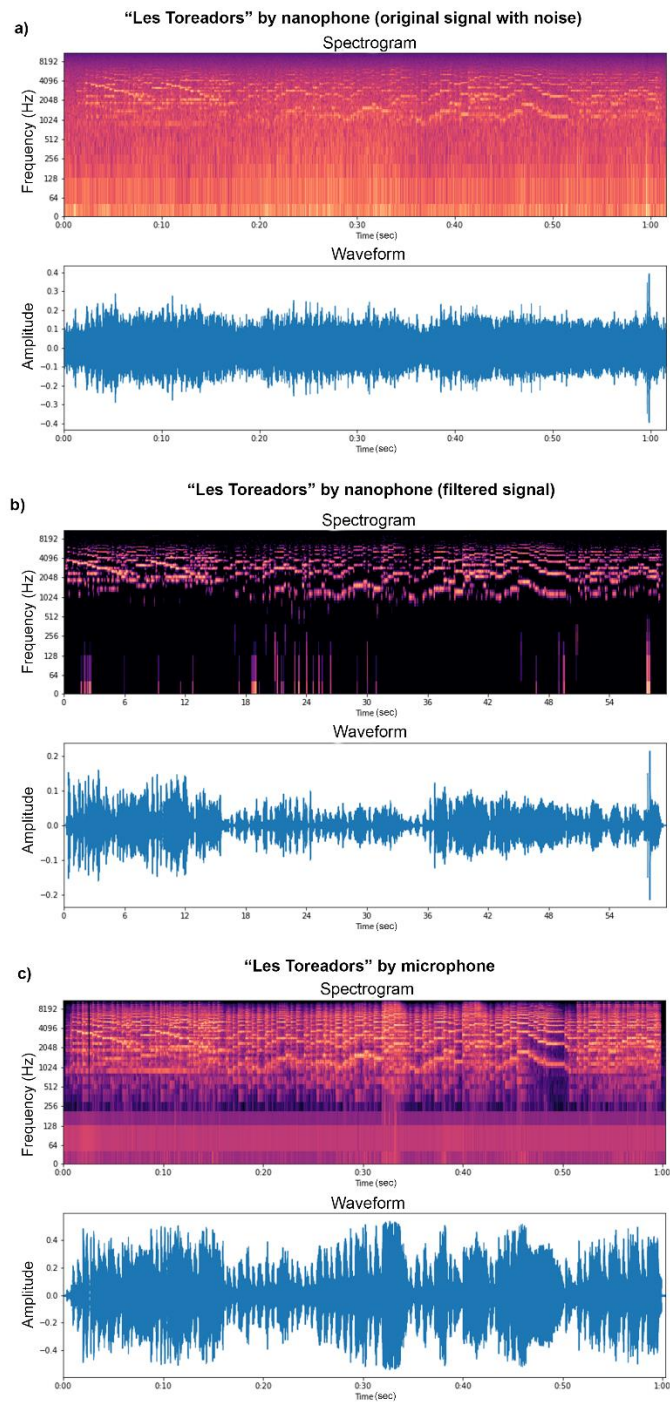
Figure 31. "Les Toreadors" recordings by nanophone and microphone. (a) Original signal of "Les Toreadors" recorded by nanophone, its spectrogram and the waveform. (b) The spectrogram and the waveform of the filtered "Les Toreadors" signal, recorded by nanophone. (c) The spectrogram and the waveform of the filtered "Les Toreadors" signal, recorded by a microphone.

3.4.5. Passive electrical elements

In addition to the applications mentioned above, CNT fibers, produced by the WP method, are successfully utilized as passive electrical elements. We demonstrated a flexible electrical diode circuit prototype, made with the use of SWCNT fibers as conductive wires (see **Figure 32** and video in operation <u>https://youtu.be/jbuRyvEdmro)</u>

The flexible electronic circuit was made using SWCNT fibers as conductive wires. First, a thin PDMS film was prepared and cured. Then diodes and a controller were placed on it upside down. Next, diodes and a microcontroller were connected with the WP fibers, using a conductive epoxy (CircuitWorks® Conductive Epoxy). Finally, the whole circuit was covered with a liquid PDMS layer to fix the position of fibers and components and then cured.
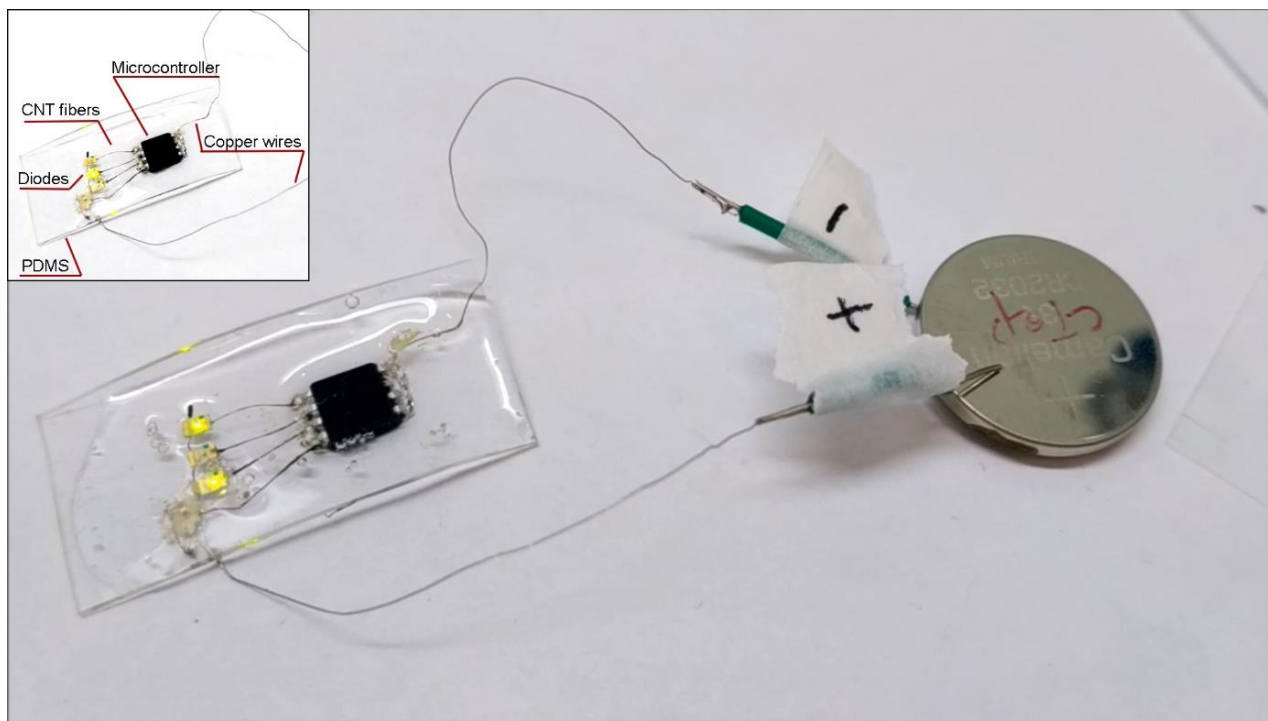
Figure 32. Electrical circuit with the WP SWCNT fiber utilized as wires.

Opportunities for other applications for WP fiber. A wide range of applications of these WP produced CNT fibers is not limited to those reported in this work. The mechanical and electrical properties of such fibers suggest potential uses in a broad range of

various devices. In the WP method, properties of fibers, such as diameters and length, electrical conductivity, tensile strength, etc., are directly dependent on the initial CNT film dimensions. By varying those parameters, it is straightforward to obtain fibers with desired characteristics. The WP method is expected to be useful for researchers as well as engineers, who need a fast, cheap, and straightforward technique of the CNT fiber production and rapid prototyping of flexible and stretchable devices. We hope that the WP method, proposed in this study, will enhance CNT fiber investigation and its utilization in science and technology.

3.5. Sensor enhancements

3.5.1. Light feedback

Encapsulated WP fiber-based sensor can be used in various conditions, including underwater and even some radiation environments. Sometimes it is difficult or even impossible for a person to be near, but he controls remotely. For such purposes, the light feedback was designed for the WP sensor (**Figure 33**). One can see the video of the sensor in operation here https://youtu.be/vPavrI7fCfg. The embedded LED changes its color according to the force applied.
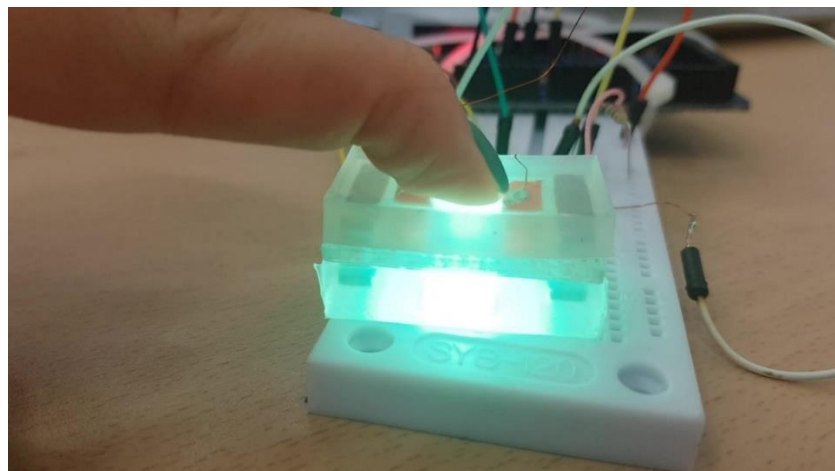
Figure 33. WP SWCNT based sensor with the light feedback in operation. Snapshot from the video.

Manufacturing process. Developmental stages of the sensor parts are descriptively detailed in **Figure 21**. Because of the bending void, the special 3-parts mold was designed and 3D printed (**Figure 34**). We utilize 3D printed parts for the base of the mold while the sensitive top layer (**Figure 35**) could be quickly produced using stages of PDMS.
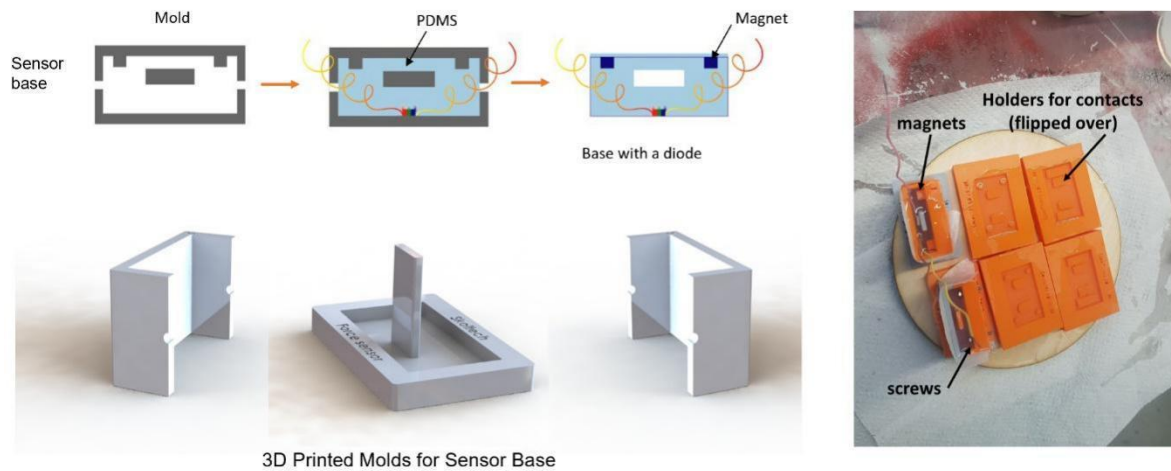
Figure 34. Sensor base development and molding stages for the base of the sensor.
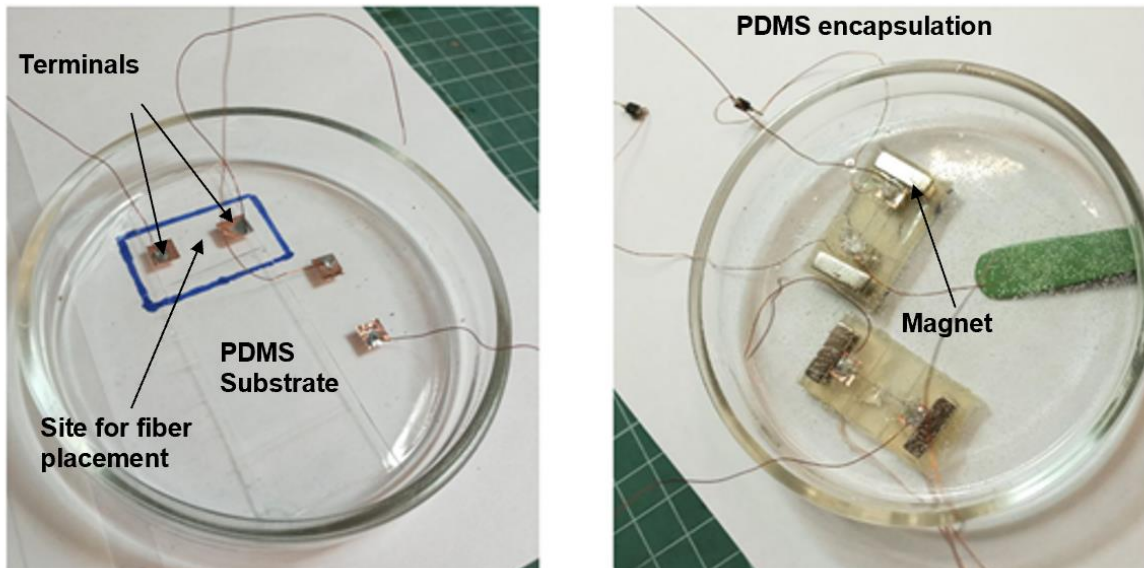
Figure 35. Sensor top layer development containing the sensitive fiber PDMS encapsulation procedures.

The electrical circuit for the LED light feedback. The electrical scheme shown in **Figure 36** allows for the creation of a sensor with visual feedback. V_{out} is connected to an Arduino microcontroller ADC (not shown), which is used to read the voltage and to control the brightness of the LED. The range of the Arduino ADC is from 0 to 5 V. The purpose of the circuit is to increase the measurement precision in the operational region by mapping this region to the full input range of the used ADC. It is possible since the changes of the resistance of the fiber do not typically exceed 10% (sensitivity) of the initial resistance. The schematic could also function in operability as a tactile sensor as demonstrated in S4.
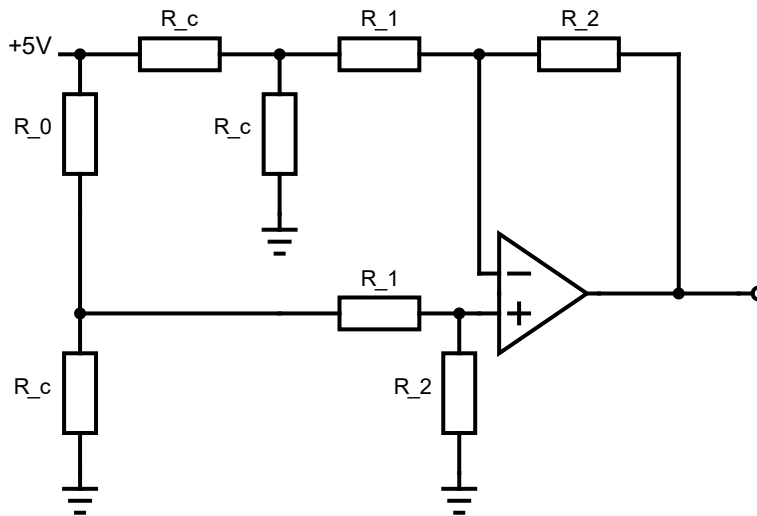
Figure 36. Sensor electrical circuit for the LED. R_0 and R_c are both the fiber resistance and comparative resistor (similar resistance as the pristine fiber), R_1 and R_2 are auxiliary resistances to tune the amplification coefficient, V_{out} is measured by an ADC, the resulting value is scaled appropriately and displayed with the brightness of the LED.

The circuit includes a differential voltage amplifier using an operational amplifier, and a voltage divider to allocate a potential to compare to the resistance R_0 of the fiber changes. The output voltage formula is

$$V_{out} = V_{max} \frac{R_2}{R_1} [\frac{R_0}{R_0 + R_c} - \frac{1}{2}],$$ (18)

where V_{out} is the output voltage, which can be read by the ADC, the resulting value is scaled appropriately and displayed with the brightness of the LED. It is scaled linearly in such a way, that the maximum force corresponds to the full LED brightness, and the absence of force corresponds to 0 brightness. R_0 and R_c are the fiber resistance and comparative resistor (similar resistance as the pristine fiber), V_{max} is the voltage of the power source and the ADC range upper boundary, R_2 and R_1 are auxiliary resistances, used to select the amplification coefficient.

3.5.2. Adjustable force range

In order for the sensor to be universal for different loads, the author came up with the design of the stiffeners' plates, which can be easily exchanged. Utilizing stiffeners (**Figure 37**) changes the stiffness coefficient of the sensor and as a result tunes the force range. Thus the thickness, density and materials can be changed according to the need.

Thickness 1 mm   Thickness 1 mm   Thickness 1.5 mm   Thickness 1.25 mm
Density 50%   Density 90%   Density 80%   Density 90%
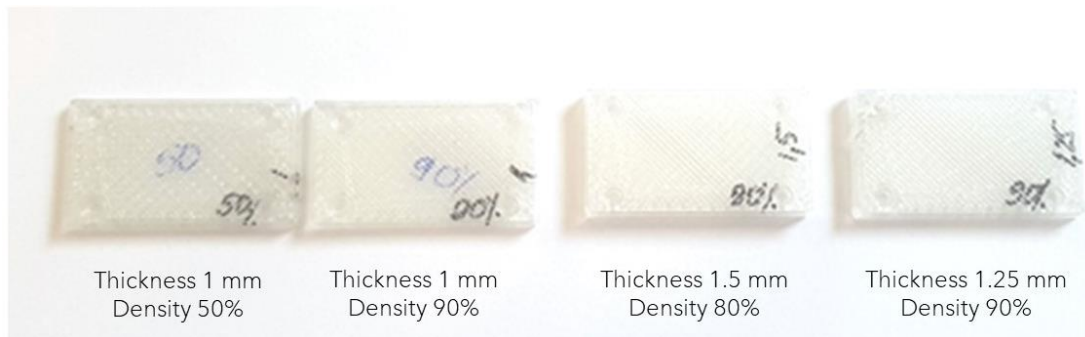
Figure 37. Stiffener plates of different thickness and density.

The design of the adjustable force sensor is fully described in Figures **26d,e**. As was mentioned in chapter 3.4.1 two designs (screw- and magnet-based) were developed (**Figure 38**). The stiffener plates are located between the base and the sensitive layer.
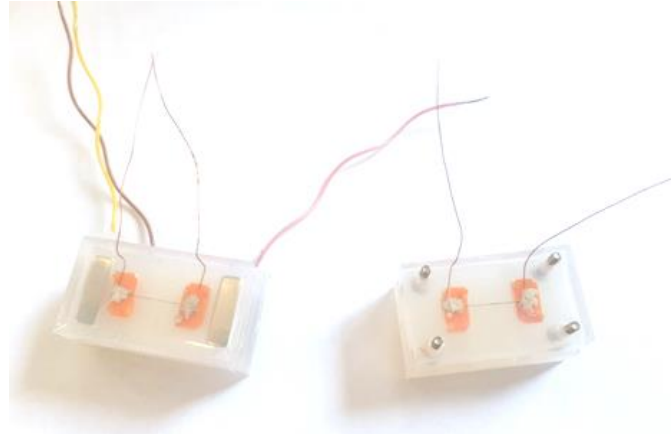
Figure 38. Two designs of the adjustable force sensor: magnet-based (left) and screw-based (right).

The major goal of the magnets and screws is to hold the stiffener plate, while it can be easily changed to another one, to serve the application needs.

Figure 39 demonstrated the soundness of our earlier assumption using the linear spring model to linearize stress-induced around the sensor geometry. Load parameters from the stiffener materials were adequately evaluated based on the beam to spring model discussed and based on the force sensor principle of operation. Spring model equivalence graph **Figure 24b** with the linear fit (R^2 = 0.99959) shows conformance to the linear, mechanistic model from experimental data with stiffener made from FLEX, TPU & PLA (3D printer plastics from rec3Dcompany[1]. The load detection limit of the force sensor with an adjustable stiffener thickness (corresponding to increasing stiffness). From the set of stiffeners evaluated, a few were selected to evaluate the force sensing ranges of the adjustable force-sensing architectures. Taking TPU plates and a selected pick of PLA and Flex 3D (flexible plastic) printed polyplastics were examined. The 3D printer materials were acquired from rec3D, Russia.

---

[1] 3D printing materials: https://rec3d.ru/en/
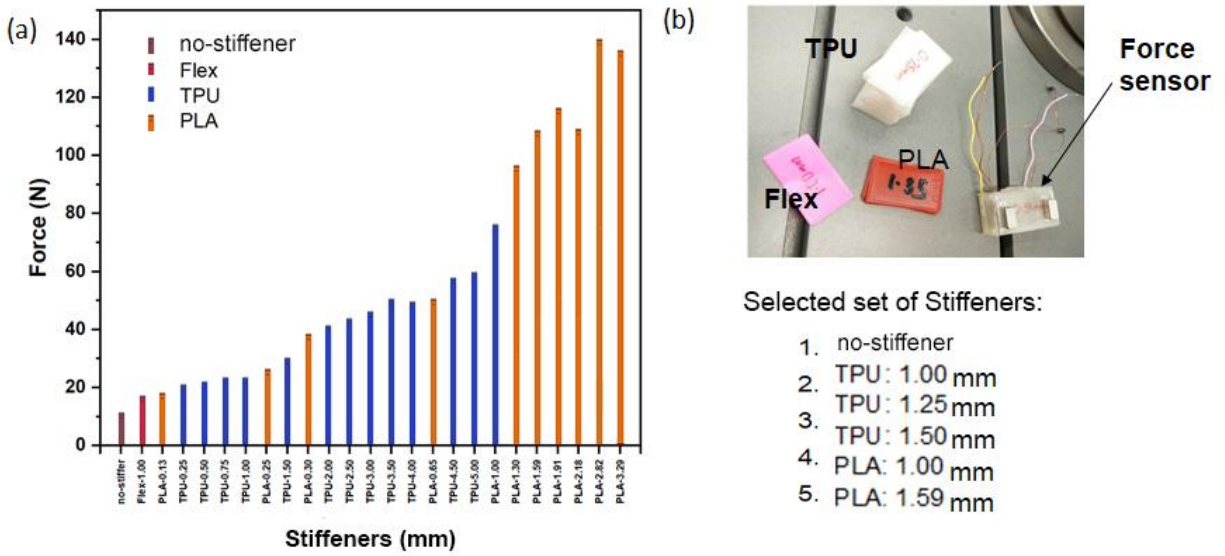
Figure 39: (a) Mechanical characterization of stiffener samples. (b) The photograph of the selected stiffeners' materials with different thicknesses.

4. Conclusions

Thus, a novel technique for CNT fiber fabrication has been developed. It is a universal method for both low-cost manufacturing and rapid prototyping. The WP method can be scaled by using a roll-to-roll production. By varying parameters of the CNT films, we demonstrated the possibility to control the strength of the SWCNT fibers from 300 to 700 MPa and their resistance from 60 to 300 Ohm (for 1 cm long fiber).

The performance of the produced WP fibers was enhanced by using various solvents (ethanol, acetone, DMSO and THF), dopant ($HAuCl_4$) and applying twisting. In principle, the possibility of functionalization and doping of CNT films before folding them into a fiber is an advantage of the WP method over other approaches, since this provides the best opportunity to obtain a uniform distribution of the introduced impurities throughout the fiber volume. Fibers formed using ethanol demonstrate the lowest packing degree f = 0.023 with respect to a reference densely packed SWCNT bundle. After twisting, the average value of f increases to 0.15. The measured fiber conductivities can be described by a linear dependence on packing degree, $\sigma_e = kf$, with the slope coefficient k of $5.0 \cdot 10^3$ and $1.0 \cdot 10^4$ S/cm for the pristine and doped fibers, respectively. The fibers obtained using acetone have the largest packing density compared to fibers prepared with the other tested liquids, which can be attributed to the high evaporation rate of acetone from the CNT film surface during the fiber formation. THF gives fibers with significantly higher resistance compared to those prepared with acetone, ethanol or DMSO. The reason for this seems to be that the adsorbed THF molecules on the CNT walls weaken the inter bundle electrical conductivity. The highest values of toughness have been obtained for fibers treated in the solutions of $HAuCl_4$ in ethanol (127 J/g at 23% fracture strain) and acetone (103 J/g at 22% fracture strain). The resistance sensitivity to strain was found to be dependent on mechanical processing and chemical treatment. The varies between 0.2 and 14, depending on the fiber twisting and doping. Thus, the physical properties of the fibers produced by the WP method can be tuned to suit different applications in electronics.

The produced fibers have a wide range of potential applications. We utilized them to build a force sensor, vibration monitor, a pulsometer, a nanophone and passive electrical components for the diode circuit. While annexing piezoresistive properties of the wet pulled SWCNT fibers under strain, we can measure the force applied and the deflection of the structure by measuring the fiber resistance. The force range can be tuned by changing the modulus with the stiffener plates. We benchmarked our force sensor with a safe deflection limit of 2.5 mm to allow for reliability and longer service life (> 10000 cycles). Using longer fibers and another sensor architecture facilitates increases of the deflection limit. Fiber PDMS encapsulation opens up the opportunity for broad applications, e.g. underwater, bio-compatible, light feedback implementation, and increases the size of the sensor for comfortable usage. Furthermore, with the selection of different stiffener materials (thin plate stiffeners), load limit ranges can be increased from 1.2 to 104 N, close to two orders of magnitude increase from the nominal limit of the sensor alone which allows to measure up to 10 N. In addition, we demonstrate the quick response of the sensor, by recording the music and testing it as a vibration monitor. Good merits, while simple production, gives the sensor a great potential for the rapid prototyping of sensitive flexible fiber-based devices for soft robotics to be employed as touch, displacement, and force sensors.

5. Bibliography

(1)   O'Connell, M. *Carbon Nanotubes: Properties and Applications*; CRC/Taylor & Francis, 2006.

(2)   Zhang, M.; Atkinson, K. R.; Baughman, R. H. Multifunctional Carbon Nanotube Yarns by Downsizing an Ancient Technology. *Science* **2004**, *306* (5700), 1358–1361.

(3)   Shaikh, S.; Li, L.; Lafdi, K.; Huie, J. Thermal Conductivity of an Aligned Carbon Nanotube Array. *Carbon* **2007**, *45* (13), 2608–2613.

(4)   Nasibulin, A. G.; Kaskela, A.; Mustonen, K.; Anisimov, A. S.; Ruiz, V.; Kivistö, S.; Rackauskas, S.; Timmermans, M. Y.; Pudas, M.; Aitchison, B.; et al. Multifunctional Free-Standing Single-Walled Carbon Nanotube Films. *ACS Nano* **2011**, *5* (4), 3214–3221.

(5)   Mylvaganam, K.; Zhang, L. C. Ballistic Resistance Capacity of Carbon Nanotubes. *Nanotechnology* **2007**, *18* (47), 475701.

(6)   Nasouri, K.; Shoushtari, A. M. Designing, Modeling and Manufacturing of Lightweight Carbon Nanotubes/Polymer Composite Nanofibers for Electromagnetic Interference Shielding Application. *Compos. Sci. Technol.* **2017**, *145*, 46–54.

(7)   Gonzalez, G.; Chiappone, A.; Roppolo, I.; Fantino, E.; Bertana, V.; Perrucci, F.; Scaltrito, L.; Pirri, F.; Sangermano, M. Development of 3D Printable Formulations Containing CNT with Enhanced Electrical Properties. *Polymer (Guildf).* **2017**, *109*, 246–253.

(8)   Novikov, L. S.; Voronina, E. N. Potential Space Applications of Nanomaterials; Springer, Cham, 2017; pp 139–147.

(9)   Shim, B. S.; Chen, W.; Doty, C.; Xu, C.; Kotov, N. A. Smart Electronic Yarns and Wearable Fabrics for Human Biomonitoring Made by Carbon Nanotube

Coating with Polyelectrolytes. *Nano Lett.* **2008**, *8* (12), 4151–4157.

(10)   Zeng, W.; Shu, L.; Li, Q.; Chen, S.; Wang, F.; Tao, X.-M. Fiber-Based Wearable Electronics: A Review of Materials, Fabrication, Devices, and Applications. *Adv. Mater.* **2014**, *26* (31), 5310–5336.

(11)   Aitola, K.; Domanski, K.; Correa-Baena, J.-P.; Sveinbjörnsson, K.; Saliba, M.; Abate, A.; Grätzel, M.; Kauppinen, E.; Johansson, E. M. J.; Tress, W.; et al. High Temperature-Stable Perovskite Solar Cell Based on Low-Cost Carbon Nanotube Hole Contact. *Adv. Mater.* **2017**, *29* (17), 1606398.

(12)   Xu, W.; Wu, S.; Li, X.; Zou, M.; Yang, L.; Zhang, Z.; Wei, J.; Hu, S.; Li, Y.; Cao, A. High-Efficiency Large-Area Carbon Nanotube-Silicon Solar Cells. *Adv. Energy Mater.* **2016**, *6* (12), 1–9.

(13)   Tang, R.; Shi, Y.; Hou, Z.; Wei, L. Carbon Nanotube-Based Chemiresistive Sensors. *Sensors* **2017**, *17* (4), 882.

(14)   Goya, K.; Fuchiwaki, Y.; Tanaka, M.; Addinall, R.; Ooie, T.; Sugino, T.; Asaka, K. A Micropipette System Based on Low Driving Voltage Carbon Nanotube Actuator. *Microsyst. Technol.* **2017**, *23* (7), 2657–2661.

(15)   Qu, G.; Cheng, J.; Li, X.; Yuan, D.; Chen, P.; Chen, X.; Wang, B.; Peng, H. A Fiber Supercapacitor with High Energy Density Based on Hollow Graphene/Conducting Polymer Fiber Electrode. *Adv. Mater.* **2016**, *28* (19), 3646–3652.

(16)   Wang, Z.; Zhang, L.; Bayram, Y.; Volakis, J. L. Embroidered Conductive Fibers on Polymer Composite for Conformal Antennas. *IEEE Trans. Antennas Propag.* **2012**, *60* (9), 4141–4147.

(17)   Cheng, H.; Dong, Z.; Hu, C.; Zhao, Y.; Hu, Y.; Qu, L.; Chen, N.; Dai, L. Textile Electrodes Woven by Carbon Nanotube–Graphene Hybrid Fibers for Flexible Electrochemical Capacitors. *Nanoscale* **2013**, *5* (8), 3428.

(18)   Gilshteyn, E.; Nasibulin, A. G. Aerosol Synthesized Carbon Nanotube Films for Stretchable Electronic Applications. In *2015 IEEE 15th International Conference on Nanotechnology (IEEE-NANO)*; IEEE, 2015; pp 893–896.

(19)   Sundaram, R. M.; Windle, A. H. One-Step Purification of Direct-Spun CNT Fibers by Post-Production Sonication. *Mater. Des.* **2017**, *126*, 85–90.

(20)   He, S.; Hu, Y.; Wan, J.; Gao, Q.; Wang, Y.; Xie, S.; Qiu, L.; Wang, C.; Zheng, G.; Wang, B.; et al. Biocompatible Carbon Nanotube Fibers for Implantable Supercapacitors. *Carbon* **2017**, *122*, 162–167.

(21)   Yadav, M. D.; Dasgupta, K.; Patwardhan, A. W.; Joshi, J. B. High Performance Fibers from Carbon Nanotubes: Synthesis, Characterization, and Applications in Composites–A Review. *Ind. Eng. Chem. Res.* **2017**, *56* (44), 12407–12437.

(22)   Di, J.; Zhang, X.; Yong, Z.; Zhang, Y.; Li, D.; Li, R.; Li, Q. Carbon-Nanotube Fibers for Wearable Devices and Smart Textiles. *Adv. Mater.* **2016**, *28* (47), 10529–10538.

(23)   Vigolo, B.; Pénicaud, A.; Coulon, C.; Sauder, C.; Pailler, R.; Journet, C.; Bernier, P.; Poulin, P. Macroscopic Fibers and Ribbons of Oriented Carbon Nanotubes. *Science* **2000**, *290* (5495), 1331–1334.

(24)   Janas, D.; Koziol, K. K. Carbon Nanotube Fibers and Films: Synthesis, Applications and Perspectives of the Direct-Spinning Method. *Nanoscale* **2016**, *8* (47), 19475–19490.

(25)   Lee, S.-H.; Kim, H.-R.; Lee, T.; Lee, H.; Lee, J.; Lee, J.; Park, J.; Lee, K.-H. Synthesis of Carbon Nanotube Fibers from Carbon Precursors with Low Decomposition Temperatures Using a Direct Spinning Process. *Carbon* **2017**, *124*, 219–227.

(26)   Wang, J. N.; Luo, X. G.; Wu, T.; Chen, Y. High-Strength Carbon Nanotube Fibre-like Ribbon with High Ductility and High Electrical Conductivity. *Nat. Commun.* **2014**, *5*, 1–8.

(27) Yu, X.; Zhang, X.; Zou, J.; Lan, Z.; Jiang, C.; Zhao, J.; Zhang, D.; Miao, M.; Li, Q. Solvent-Tunable Microstructures of Aligned Carbon Nanotube Films. *Adv. Mater. Interfaces* **2016**, *3* (17), 1–6.

(28) Ericson, L. M.; Fan, H.; Peng, H.; Davis, V. A.; Zhou, W.; Sulpizio, J.; Wang, Y.; Booker, R.; Vavro, J.; Guthy, C.; et al. Macroscopic, Neat, Single-Walled Carbon Nanotube Fibers. *Science* **2004**, *305* (5689), 1447–1450.

(29) Taylor, L. W.; Dewey, O. S.; Headrick, R. J.; Komatsu, N.; Peraca, N. M.; Wehmeyer, G.; Kono, J.; Pasquali, M. Improved Properties, Increased Production, and the Path to Broad Adoption of Carbon Nanotube Fibers. *Carbon* **2021**, *171*, 689–694.

(30) Lee, J.; Lee, D.-M.; Jung, Y.; Park, J.; Lee, H. S.; Kim, Y.-K.; Park, C. R.; Jeong, H. S.; Seung, &; Kim, M. Direct Spinning and Densification Method for High-Performance Carbon Nanotube Fibers.

(31) Liu, K.; Sun, Y.; Zhou, R.; Zhu, H.; Wang, J.; Liu, L.; Fan, S.; Jiang, K. Carbon Nanotube Yarns with High Tensile Strength Made by a Twisting and Shrinking Method. *Nanotechnology* **2009**, *21* (4), 45708.

(32) Li, S.; Zhang, X.; Zhao, J.; Meng, F.; Xu, G.; Yong, Z.; Jia, J.; Zhang, Z.; Li, Q. Enhancement of Carbon Nanotube Fibres Using Different Solvents and Polymers. *Compos. Sci. Technol.* **2012**, *72* (12), 1402–1407.

(33) Zhilyaeva, M. A.; Shulga, E. V.; Shandakov, S. D.; Sergeichev, I. V.; Gilshteyn, E. P.; Anisimov, A. S.; Nasibulin, A. G. A Novel Straightforward Wet Pulling Technique to Fabricate Carbon Nanotube Fibers. *Carbon* **2019**, *150*, 69–75.

(34) Cheng, M.; Zhu, G.; Zhang, F.; Tang, W. lai; Jianping, S.; Yang, J. quan; Zhu, L. ya. A Review of Flexible Force Sensors for Human Health Monitoring. *Journal of Advanced Research*. Elsevier B.V. November 1, 2020, pp 53–68.

(35) Templeman, J. O.; Sheil, B. B.; Sun, T. Multi-Axis Force Sensors: A State-of-the-Art Review. *Sensors and Actuators, A: Physical*. Elsevier B.V. April 1, 2020, p

111772.

(36)   Zhang, B.; Xie, Y.; Zhou, J.; Wang, K.; Zhang, Z. State-of-the-Art Robotic Grippers, Grasping and Control Strategies, as Well as Their Applications in Agricultural Robots: A Review. *Computers and Electronics in Agriculture*. Elsevier B.V. October 1, 2020, p 105694.

(37)   Ilami, M.; Bagheri, H.; Ahmed, R.; Skowronek, E. O.; Marvi, H. Materials, Actuators, and Sensors for Soft Bioinspired Robots. *Adv. Mater.* **2020**, 2003139.

(38)   Sorrentino, I.; Chavez, F. J. A.; Latella, C.; Fiorio, L.; Traversaro, S.; Rapetti, L.; Tirupachuri, Y.; Guedelha, N.; Maggiali, M.; Dussoni, S.; et al. A Novel Sensorised Insole for Sensing Feet Pressure Distributions. *Sensors (Switzerland)* **2020**, *20* (3), 747.

(39)   Choi, W. H.; Kim, S.; Lee, D.; Shin, D. Soft, Multi-DoF, Variable Stiffness Mechanism Using Layer Jamming for Wearable Robots. *IEEE Robot. Autom. Lett.* **2019**, *4* (3), 2539–2546.

(40)   Cao, P.-J.; Liu, Y.; Asghar, W.; Hu, C.; Li, F.; Wu, Y.; Li, Y.; Yu, Z.; Li, S.; Shang, J.; et al. A Stretchable Capacitive Strain Sensor Having Adjustable Elastic Modulus Capability for Wide-Range Force Detection. *Adv. Eng. Mater.* **2020**, *22* (3), 1901239.

(41)   Gilshteyn, E. P.; Romanov, S. A.; Kopylova, D. S.; Savostyanov, G. V.; Anisimov, A. S.; Glukhova, O. E.; Nasibulin, A. G. Mechanically Tunable Single-Walled Carbon Nanotube Films as a Universal Material for Transparent and Stretchable Electronics. *ACS Appl. Mater. Interfaces* **2019**, *11* (30), 27327–27334.

(42)   Iida, F.; Laschi, C. Soft Robotics: Challenges and Perspectives. In *Procedia Computer Science*; Elsevier B.V., 2011; Vol. 7, pp 99–102.

(43)   Majidi, C. Soft Robotics: A Perspective - Current Trends and Prospects for the Future. *Soft Robotics*. Mary Ann Liebert Inc. March 2014, pp 5–11.

(44) Chi, C.; Sun, X.; Xue, N.; Li, T.; Liu, C. Recent Progress in Technologies for Tactile Sensors. *Sensors (Switzerland)*. MDPI AG March 2018, p 948.

(45) Xiao, Z. G.; Menon, C. A Review of Force Myography Research and Development. *Sensors (Switzerland)*. MDPI AG October 2019, p 4557.

(46) Nie, B.; Yao, T.; Zhang, Y.; Liu, J.; Chen, X. A Droplet-Based Passive Force Sensor for Remote Tactile Sensing Applications. *Appl. Phys. Lett.* **2018**, *112* (3), 031904.

(47) Pan, S.; Liu, Z.; Wang, M.; Jiang, Y.; Luo, Y.; Wan, C.; Qi, D.; Wang, C.; Ge, X.; Chen, X. Mechanocombinatorially Screening Sensitivity of Stretchable Strain Sensors. *Adv. Mater.* **2019**, *31* (35), 1903130.

(48) Duan, J.; Liang, X.; Guo, J.; Zhu, K.; Zhang, L. Ultra-Stretchable and Force-Sensitive Hydrogels Reinforced with Chitosan Microspheres Embedded in Polymer Networks. *Adv. Mater.* **2016**, *28* (36), 8037–8044.

(49) Zhu, Y.; Li, J.; Cai, H.; Wu, Y.; Ding, H.; Pan, N.; Wang, X. Highly Sensitive and Skin-like Pressure Sensor Based on Asymmetric Double-Layered Structures of Reduced Graphite Oxide. *Sensors Actuators, B Chem.* **2018**, *255*, 1262–1267.

(50) Souri, H.; Bhattacharyya, D. Wearable Strain Sensors Based on Electrically Conductive Natural Fiber Yarns. *Mater. Des.* **2018**, *154*, 217–227.

(51) Cutkosky, M. R.; Howe, R. D.; Provancher, W. R. Force and Tactile Sensors. In *Springer Handbook of Robotics*; Springer Berlin Heidelberg: Berlin, Heidelberg, 2008; pp 455–476.

(52) Li, J.; Liu, H.; Althoefer, K.; Seneviratne, L. D. A Stiffness Probe Based on Force and Vision Sensing for Soft Tissue Diagnosis. In *Proceedings of the Annual International Conference of the IEEE Engineering in Medicine and Biology Society, EMBS*; 2012; Vol. 2012, pp 944–947.

(53) Rogers, J. A.; Someya, T.; Huang, Y. Materials and Mechanics for Stretchable

Electronics. *Science*. Science March 2010, pp 1603–1607.

(54)   Cheng, S.; Wu, Z. Microfluidic Electronics. *Lab on a Chip*. Royal Society of Chemistry August 2012, pp 2782–2791.

(55)   Xi, X.; Chung, D. D. L. Capacitance-Based Self-Sensing of Flaws and Stress in Carbon-Carbon Composites, with Reports of the Electric Permittivity, Piezoelectricity and Piezoresistivity. *Carbon* **2019**, *146*, 447–461.

(56)   Chung, D. D. L. A Review of Multifunctional Polymer-Matrix Structural Composites. *Compos. Part B Eng.* **2019**, *160*, 644–660.

(57)   Zhang, X.; Kow, J.; Jones, D.; de Boer, G.; Ghanbari, A.; Serjouei, A.; Culmer, P.; Alazmani, A. Adjustable Compliance Soft Sensor via an Elastically Inflatable Fluidic Dome. *Sensors* **2021**, *21* (6), 1–15.

(58)   Zeng, X.; Hurd, C.; Su, H. J.; Song, S.; Wang, J. A Parallel-Guided Compliant Mechanism with Variable Stiffness Based on Layer Jamming. *Mech. Mach. Theory* **2020**, *148*, 103791.

(59)   Nasibulin, A. G.; Moisala, A.; Brown, D. P.; Jiang, H.; Kauppinen, E. I. A Novel Aerosol Method for Single Walled Carbon Nanotube Synthesis. *Chem. Phys. Lett.* **2005**, *402* (1–3), 227–232.

(60)   Moisala, A.; Nasibulin, A. G.; Brown, D. P.; Jiang, H.; Khriachtchev, L.; Kauppinen, E. I. Single-Walled Carbon Nanotube Synthesis Using Ferrocene and Iron Pentacarbonyl in a Laminar Flow Reactor. *Chem. Eng. Sci.* **2006**, *61* (13), 4393–4402.

(61)   Moisala, A.; Nasibulin, A. G.; Shandakov, S. D.; Jiang, H.; Kauppinen, E. I. On-Line Detection of Single-Walled Carbon Nanotube Formation during Aerosol Synthesis Methods. *Carbon* **2005**, *43* (10), 2066–2074.

(62)   Odom, T. W.; Huang, J.-L.; Kim, P.; Lieber, C. M. Atomic Structure and Electronic Properties of Single-Walled Carbon Nanotubes. *Nature* **1998**, *391*

(6662), 62–64.

(63) Romanov, S. A.; Aliev, A. E.; Fine, B. V.; Anisimov, A. S.; Nasibulin, A. G. Highly
      Efficient Thermophones Based on Freestanding Single-Walled Carbon
      Nanotube Films. *Nanoscale Horizons* **2019**, *4* (5), 1158–1163.

(64) Kanninen, P.; Luong, N. D.; Sinh, L. H.; Anoshkin, I. V.; Tsapenko, A.; Seppälä, J.;
      Nasibulin, A. G.; Kallio, T. Transparent and Flexible High-Performance
      Supercapacitors Based on Single-Walled Carbon Nanotube Films.
      Nanotechnology **2016**, *27* (23), 1–6.

(65) Ermolaev, G. A.; Tsapenko, A. P.; Volkov, V. S.; Anisimov, A. S.; Gladush, Y. G.;
      Nasibulin, A. G. Express Determination of Thickness and Dielectric Function of
      Single-Walled Carbon Nanotube Films. *Appl. Phys. Lett.* **2020**, *116* (23),
      231103.

(66) Zhilyaeva, M. A.; Shulga, E. V.; Shandakov, S. D.; Sergeichev, I. V.; Gilshteyn, E.
      P.; Anisimov, A. S.; Nasibulin, A. G. A Novel Straightforward Wet Pulling
      Technique to Fabricate Carbon Nanotube Fibers. *Carbon* **2019**, *150*, 69–75.

(67) Mikheev, G. M.; Nasibulin, A. G.; Zonov, R. G.; Kaskela, A.; Kauppinen, E. I.
      Photon-Drag Effect in Single-Walled Carbon Nanotube Films. *Nano Lett.* **2012**,
      12 (1), 77–83.

(68) Wei, Y.; Jiang, K.; Feng, X.; Liu, P.; Liu, L.; Fan, S. Comparative Studies of
      Multiwalled Carbon Nanotube Sheets before and after Shrinking. *Phys. Rev. B*
      2007, *76* (4), 045423.

(69) Liu, K.; Sun, Y.; Liu, P.; Zhou, R.; Zhu, H.; Wang, J.; Liu, L.; Fan, S.; Jiang, K.
      Carbon Nanotube Yarns with High Tensile Strength Made by a Twisting and
      Shrinking Method. *IOP Publ. Nanotechnol. Nanotechnol.* **2010**, *21*, 45708–7.

(70) Kaskela, A.; Nasibulin, A. G.; Timmermans, M. Y.; Aitchison, B.; Papadimitratos,
      A.; Tian, Y.; Zhu, Z.; Jiang, H.; Brown, D. P.; Zakhidov, A.; et al. Aerosol-
      Synthesized SWCNT Networks with Tunable Conductivity and Transparency by

a Dry Transfer Technique. *Nano Lett.* **2010**, *10* (11), 4349–4355.

(71)   Tawfick, S.; De Volder, M.; Hart, A. J. Structurally Programmed Capillary Folding of Carbon Nanotube Assemblies. **2011**, *27*, 6389–6394.

(72)   Tawfick, S.; De Volder, M.; Hart, A. J. Structurally Programmed Capillary Folding of Carbon Nanotube Assemblies. *Langmuir* **2011**, *27* (10), 6389–6394.

(73)   Atkinson, K. R.; Hawkins, S. C.; Huynh, C.; Skourtis, C.; Dai, J.; Zhang, M.; Fang, S.; Zakhidov, A. A.; Lee, S. B.; Aliev, A. E.; et al. Multifunctional Carbon Nanotube Yarns and Transparent Sheets: Fabrication, Properties, and Applications. *Phys. B Condens. Matter* **2007**, *394* (2), 339–343.

(74)   Headrick, R. J.; Tsentalovich, D. E.; Berdegué, J.; Bengio, E. A.; Liberman, L.; Kleinerman, O.; Lucas, M. S.; Talmon, Y.; Pasquali, M. Structure-Property Relations in Carbon Nanotube Fibers by Downscaling Solution Processing. *Adv. Mater.* **2018**, *30* (9), 1704482.

(75)   Miao, M. Electrical Conductivity of Pure Carbon Nanotube Yarns. *Carbon* **2011**, *49* (12), 3755–3761.

(76)   Can-Ortiz, A.; Abot, J. L.; Avilés, F. Electrical Characterization of Carbon-Based Fibers and Their Application for Sensing Relaxation-Induced Piezoresistivity in Polymer Composites. *Carbon* **2019**, *145*, 119–130.

(77)   Anike, J. C.; Belay, K.; Abot, J. L. Effect of Twist on the Electromechanical Properties of Carbon Nanotube Yarns. *Carbon* **2019**, *142*, 491–503.

(78)   Fernández-Toribio, J. C.; Alemán, B.; Ridruejo, Á.; Vilatela, J. J. Tensile Properties of Carbon Nanotube Fibres Described by the Fibrillar Crystallite Model. *Carbon* **2018**, *133*, 44–52.

(79)   Yu, X.; Zhao, J.; Zhao, T.; Li, S.; Zhang, X.; Li, Q.; Liu, F.; Gao, P.; Han, Y.; Zhang, Y. Bio-Inspired Aggregation Control of Carbon Nanotubes for Ultra-Strong Composites. *Sci. Rep.* **2015**, *5* (1), 1–9.

(80) Koziol, K.; Vilatela, J.; Moisala, A.; Motta, M.; Cunniff, P.; Sennett, M.; Windle, A. High-Performance Carbon Nanotube Fiber. *Science (80-.).* **2007**, *318* (5858), 1892–1895.

(81) Vilatela, J. J.; Elliott, J. A.; Windle, A. H. A Model for the Strength of Yarn-like Carbon Nanotube Fibers. *ACS Nano* **2011**, *5* (3), 1921–1927.

(82) Liu, J.; Lee, J. H. Self-Folding of a Slender Microbeam and Thin Film: An Elastica Model. *J. Mech. Mater. Struct.* **2013**, *3* (2–4).

(83) Lekawa-Raus, A.; Patmore, J.; Kurzepa, L.; Bulmer, J.; Koziol, K. Electrical Properties of Carbon Nanotube Based Fibers and Their Future Use in Electrical Wiring. *Adv. Funct. Mater.* **2014**, *24* (24), 3661–3682.

(84) Zhang, S.; Nguyen, N.; Leonhardt, B.; Jolowsky, C.; Hao, A.; Park, J. G.; Liang, R. Carbon-Nanotube-Based Electrical Conductors: Fabrication, Optimization, and Applications. *Advanced Electronic Materials*. Blackwell Publishing Ltd June 1, 2019, p 1800811.

(85) Lu, W.; Zu, M.; Byun, J. H.; Kim, B. S.; Chou, T. W. State of the Art of Carbon Nanotube Fibers: Opportunities and Challenges. *Advanced Materials*. John Wiley & Sons, Ltd April 10, 2012, pp 1805–1833.

(86) Dini, Y.; Faure-Vincent, J.; Carbon, J. D.-; 2019, undefined. How to Overcome the Electrical Conductivity Limitation of Carbon Nanotube Yarns Drawn from Carbon Nanotube Arrays. *Elsevier*.

(87) Han, B.; Guo, E.; Xue, X.; Zhao, Z.; Li, T.; Xu, Y.; Luo, L.; Hou, H. Enhancement of the Twisted Carbon Nanotube Fibers Properties by Drawing Processing and Acid Treatment. *Mater. Des.* **2018**, *143*, 238–247.

(88) Park, J.; Lee, J.; Lee, D. M.; Lee, S. H.; Jeong, H. S.; Lee, K. H.; Kim, S. M. Mathematical Model for the Dynamic Mechanical Behavior of Carbon Nanotube Yarn in Analogy with Hierarchically Structured Bio-Material. *Carbon* **2019**, *152*, 151–158.

(89)   Zhang, X.; Li, Q. Enhancement of Friction between Carbon Nanotubes: An Efficient Strategy to Strengthen Fibers. *ACS Nano* **2010**, *4* (1), 312–316.

(90)   Zhong, X. H.; Li, Y. L.; Liu, Y. K.; Qiao, X. H.; Feng, Y.; Liang, J.; Jin, J.; Zhu, L.; Hou, F.; Li, J. Y. Continuous Multilayered Carbon Nanotube Yarns. *Adv. Mater.* **2010**, *22* (6), 692–696.

(91)   Wu, A. S.; Nie, X.; Hudspeth, M. C.; Chen, W. W.; Chou, T. W.; Lashmore, D. S.; Schauer, M. W.; Tolle, E.; Rioux, J. Strain Rate-Dependent Tensile Properties and Dynamic Electromechanical Response of Carbon Nanotube Fibers. *Carbon* **2012**, *50* (10), 3876–3881.

(92)   Misak, H. E.; Mall, S. Electrical Conductivity, Strength and Microstructure of Carbon Nanotube Multi-Yarns. *Mater. Des.* **2015**, *75*, 76–84.

(93)   Hill, F. A.; Havel, T. F.; Lashmore, D.; Schauer, M.; Livermore, C. Storing Energy and Powering Small Systems with Mechanical Springs Made of Carbon Nanotube Yarn. *Energy* **2014**, *76*, 318–325.

(94)   Yadav, M. D.; Dasgupta, K.; Patwardhan, A. W.; Joshi, J. B. High Performance Fibers from Carbon Nanotubes: Synthesis, Characterization, and Applications in Composites - A Review. *Industrial and Engineering Chemistry Research*. American Chemical Society November 8, 2017, pp 12407–12437.

(95)   Nguyen, T. K.; Dinh, T.; Phan, H. P.; Tran, C. D.; Foisal, A. R. M.; Zhu, Y.; Dao, D. V. Electrically Stable Carbon Nanotube Yarn under Tensile Strain. *IEEE Electron Device Lett.* **2017**, *38* (9), 1331–1334.

(96)   Anike, J. C.; Belay, K.; Abot, J. L. Piezoresistive Response of Carbon Nanotube Yarns under Tension: Parametric Effects and Phenomenology. *Xinxing Tan Cailiao/New Carbon Mater.* **2018**, *33* (2), 140–154.

(97)   Yan, T.; Wang, Z.; Pan, Z.-J. Flexible Strain Sensors Fabricated Using Carbon-Based Nanomaterials: A Review. *Curr. Opin. Solid State Mater. Sci.* **2018**.

(98) Cai, J.; Chawla, S.; Naraghi, M. Piezoresistive Effect of Individual Electrospun Carbon Nanofibers for Strain Sensing. *Carbon* **2014**, *77*, 738–746.

(99) Li, Y.; Shang, Y.; He, X.; Peng, Q.; Du, S.; Shi, E.; Wu, S.; Li, Z.; Li, P.; Cao, A. Overtwisted, Resolvable Carbon Nanotube Yarn Entanglement as Strain Sensors and Rotational Actuators. *ACS Nano* **2021**, *18*, 15.

(100) Tang, Z.; Jia, S.; Wang, F.; Bian, C.; Chen, Y.; Wang, Y.; Li, B. Highly Stretchable Core−Sheath Fibers via Wet-Spinning for Wearable Strain Sensors. *ACS Appl. Mater. Interfaces* **2018**.

(101) Li, X.; Hua, T.; Xu, B. Electromechanical Properties of a Yarn Strain Sensor with Graphene-Sheath/Polyurethane-Core. *Carbon* **2017**, *118*, 686–698.

(102) Wu, X.; Han, Y.; Zhang, X.; Lu, C. Highly Sensitive, Stretchable, and Wash-Durable Strain Sensor Based on Ultrathin Conductive Layer@Polyurethane Yarn for Tiny Motion Monitoring. *ACS Appl. Mater. Interfaces* **2016**, *8* (15), 9936–9945.

(103) Yan, T.; Wang, Z.; Wang, Y. Q.; Pan, Z. J. Carbon/Graphene Composite Nanofiber Yarns for Highly Sensitive Strain Sensors. *Mater. Des.* **2018**, *143*, 214–223.

(104) Zhou, J.; Xu, X.; Yu, H.; Lubineau, G. Deformable and Wearable Carbon Nanotube Microwire-Based Sensors for Ultrasensitive Monitoring of Strain, Pressure and Torsion. *Nanoscale* **2017**, *9* (2), 604–612.

(105) Wang, Z.; Huang, Y.; Sun, J.; Huang, Y.; Hu, H.; Jiang, R.; Gai, W.; Li, G.; Zhi, C. Polyurethane/Cotton/Carbon Nanotubes Core-Spun Yarn as High Reliability Stretchable Strain Sensor for Human Motion Detection. *ACS Appl. Mater. Interfaces* **2016**, *8* (37), 24837–24843.

(106) Li, Y.; Zhou, B.; Zheng, G.; Liu, X.; Li, T.; Yan, C.; Cheng, C.; Dai, K.; Liu, C.; Shen, C.; et al. Continuously Prepared Highly Conductive and Stretchable SWNT/MWNT Synergistically Composited Electrospun Thermoplastic

Polyurethane Yarns for Wearable Sensing. *J. Mater. Chem. C* **2018**, *6* (9), 2258–2269.

6. Appendices

6.1. Audio files

In addition**,** six well-known classical melodies in a stereophonic recording were selected. Fragments of 1-minute duration with a significant amplitude difference during the recording were selected from the melodies. The fragments were downloaded to the smartphone and played from its speaker. We also conducted divider on/off test using. All nanophone music is filtered, unless otherwise stated.

[Mozart "Little Night Serenade", recorded by a commercially available microphone.](#)

[Mozart "Little Night Serenade", recorded by nanophone.](#)

[All melodies recorded by a commercially available microphone.](#)

[All melodies recorded by nanophone, with noise and divider test.](#)

[All melodies recorded by nanophone.](#)

[Paganini "Capriccio", recorded by a commercially available microphone.](#)

[Paganini "Capriccio", recorded by nanophone.](#)

[Tchaikovsky "Dance of the Little Swans", recorded by a commercially available microphone.](#)

[Tchaikovsky "Dance of the Little Swans", recorded by nanophone.](#)

[Divider test without background](#).

[Vivaldi "Seasons: Spring", recorded by a commercially available microphone.](#)

[Vivaldi "Seasons: Spring", recorded by nanophone.](#)

[Bizet "Carmen", recorded by a commercially available microphone.](#)

[Bizet "Carmen", recorded by nanophone.](#)

[Bizet "Carmen", recorded by nanophone, not filtered (with noise).](#)

[Khachaturian "Sabre Dance", recorded by a commercially available microphone.](#)

[Khachaturian "Sabre Dance", recorded by nanophone](#).